*Physics – Uspekhi* **66** (5) 437 – 459 (2023) 

*REVIEWS OF TOPICAL PROBLEMS* PACS numbers: **96.60.–j**, 96.60.Iv, 96.60.qe, 96.60.Tf

# Modern analytic models of acceleration and propagation of electrons in solar flares

P A Gritsyk, B V Somov

DOI: https://doi.org/10.3367/UFNe.2021.08.039048

## Contents



**Abstract. We review the current state of the kinetic theory of acceleration and propagation of energetic (thermal and non-thermal) electrons during solar flares. The classical models of a thick target, together with their extension to models that take the reverse current effect and the acceleration of electrons in collapsing magnetic traps into account, are discussed in detail. Analytic solutions of the corresponding kinetic equations are found and used to calculate the characteristics of the hard X-ray bremsstrahlung generated by energetic electrons. The results obtained are compared with modern high-precision data from satellite observations of solar flares. The radiation polarization degree is calculated and the prospects for its measurement in future space experiments are discussed.**

**Keywords:** Sun, solar flares, electron acceleration, kinetic equation, collision integral, bremsstrahlung, polarization

## 1. Introduction

Solar flares are the most powerful among the numerous manifestations of solar activity [1–5]. In powerful flares, a huge amount of energy, $\sim 10^{32}$ erg, is released in a short time of $\sim 10^3$ s, which corresponds to an average power of energy release of the order of $10^{29}$ erg s$^{-1}$. During the impulsive phase of a flare, the power of energy release is several times the average, and the flux of hard electromagnetic radiation from the entire Sun increases by a factor of several thousand. In invisible ultraviolet, X-, and gamma rays, the Sun flares 'brighter than a thousand suns' [6]. Within eight minutes, these rays reach Earth's orbit. Streams of charged particles accelerated to high energies and huge plasma ejections (so-called coronal mass ejections [7]) suddenly burst into interplanetary space. In space and even on Earth, solar flares represent a certain hazard [8–11].

Several energy release channels (fast magnetohydrodynamic plasma flows, powerful heat fluxes, accelerated particles, and radiation) determine the variety of physical processes caused by a flare in the solar atmosphere [12–15]. These complex and branched processes jointly contribute to the observed pattern of the flare. But the primary source of flare energy is hardly accessible to observations in the X-ray range because its emission is very low. Some progress in the study of this flare region has been achieved due to the development of techniques for processing radio spectra obtained in the range of 1–2 GHz with very high accuracy (temporal resolution of $\sim 50$ ms, spatial resolution of $\sim 1''$) [16]. For some flare events, a compact region can be localized in the corona where the primary acceleration of particles presumably occurs (see Fig. 2 in [16]), and the spatial and energy characteristics of accelerated electron beams can be studied.

According to the historically first (and still generally correct and fundamental) theoretical ideas about the mechanism of solar flares [17–23], strong magnetic fields in the solar atmosphere are the source of the flare energy. The classic studies mentioned above demonstrated the key role of magnetic reconnection, a certain type of rearrangement of magnetic field fluxes that change their topological connectivity. As a result of magnetic reconnection, the energy of interacting magnetic fluxes is converted into the kinetic

**P A Gritsyk** [(a)], **B V Somov** [(b)]
Lomonosov Moscow State University, Sternberg Astronomical Institute, Universitetskii prosp. 13, 119234 Moscow, Russian Federation
E-mail: [(a)] pgritsyk@gmail.com, [(b)] somov@sai.msu.ru

Received 28 July 2021, revised 20 August 2021
*Uspekhi Fizicheskikh Nauk* **193** (5) 465 – 490 (2023)
Translated by S Alekseev

energy of charged particles and jets — fast directed magnetohydrodynamic plasma flows.

The existence of magnetic reconnection as a fundamental mechanism of primary energy release in solar flares is currently confirmed by the data from modern satellite observations [16, 24–26], and the general picture of the flare and its scenario are believed to be understood [27–33]. Before the onset of the most powerful, so-called impulsive, phase, which lasts from several seconds to several ten seconds [34], the conditions necessary for fast magnetic reconnection are established in the corona. In the reconnection process, electrons, protons, and other ions are accelerated by the electric field inside the reconnecting high-temperature current layer to energies much higher than the thermal energies of particles in the corona and the chromosphere [35–38]. In solar flares, electrons and protons can be accelerated to high, and occasionally very high, energies: from several keV for electrons and several MeV for protons to several GeV (see, e.g., the international PAMELA experiment aboard the Russian RESURS DK-1 satellite [39, 40]).

At present, the acceleration of charged particles to high energies remains a topical problem not only in solar physics but also in modern astrophysics in general. This problem urgently needs to be solved in application to astrophysical phenomena of different scales and nature, such as

(a) magnetic reconnection in nonequilibrium magnetospheres of compact relativistic objects [41–43];

(b) gravitational collapse of stars and other astronomical objects [44, 45], for example, protostellar clouds with a frozen magnetic field [46];

(c) cosmic rays in the vicinity of Earth and in the Universe [47–49].

Solar flares are also of particular interest for a detailed study of the physical mechanisms of particle acceleration, because they can be studied in the most comprehensive way.

As is known, electrons have a much smaller mass than protons do. In the process of acceleration, they easily acquire high (nearly relativistic and relativistic) speeds. Importantly, these electrons typically have speeds much higher than the thermal ones in the plasma and carry considerable energy. We call such electrons energetic, regardless of their origin, be it thermal or nonthermal. Energetic electrons escape from the acceleration region of the reconnecting current layer and rapidly propagate along the reconnected magnetic field lines in the solar corona and the chromosphere, generating huge bursts of radiation in the hard X-ray and gamma ranges [50, 51].

Currently, a high accuracy of electromagnetic radiation receivers on spacecraft is available [52–55], which allows using the data of X-ray observations of coronal and chromospheric sources and comparing it with data in other ranges (optical, microwave, and gamma) to test existing ideas about flares and to gain insights into the fundamental mechanisms of acceleration and propagation of charged particles in astrophysical plasma.

The study of these processes during solar flares on the basis of modern observational data from space and ground-based observatories and of theoretical methods (analytic and numerical) is a key issue of fundamental importance in modern solar physics.

Section 2 is devoted to the description of modern concepts regarding the solar flare phenomenon. We formulate the kinetic problem of the propagation of energetic electrons in the solar atmosphere and discuss its classical solutions and their features. More accurate modern kinetic models of solar flares are presented in Section 3. Based on the solutions obtained, the events of December 6, 2006 and July 19, 2012 are simulated; in Section 4, these results are compared with data from X-ray observations. In Section 4, we also calculate the radiation polarization in solar flares and discuss the prospects for its measurement by ground-based and space experiments. We conclude with a discussion of the accuracy of the existing models in the context of current and future observations.

## 2. Modern concepts of solar flares

### 2.1 General picture of a solar flare

Schematically, but faithfully to the sequence of physical processes and their relative localization, a typical scenario of a solar flare can be represented as shown in Fig. 1. Plasma with a frozen-in [18] strong magnetic field flows from the solar corona into the reconnecting current layer (RCL) at a relatively low speed $\mathbf{v}_0 \sim 10$ km s$^{-1}$. Inside the current layer, the freeze-in conditions are violated, and the reconnected magnetic field lines, together with a 'superhot' (electron temperature $T_e \gtrsim 30$ MK) [29] almost collisionless plasma move out of the superhot current layer in opposite directions (mainly up and down) with speeds $\mathbf{v}_1 \sim 10^3$ km s$^{-1}$. The bremsstrahlung of superhot plasma electrons and accelerated electrons is a hard X-ray source moving in the corona [56, 57]. Under gradual cooling, the superhot plasma becomes visible in less hard X-rays. In Fig. 1, we show only the brightest part of the extended region of the entire flare, the reconnected field lines of magnetic field **B**, moving downward from the current layer at a speed $\mathbf{v}_1$ toward the chromosphere Ch and the photosphere Ph; N and S are a pair of photospheric magnetic field sources, such as sunspots.

Energetic electrons escape from the acceleration region of the reconnecting current layer and rapidly propagate along the reconnected magnetic field lines in the solar corona and the chromosphere. The density of the 'background' plasma, i.e., plasma along the propagation path of energetic electrons, varies in a wide range from $\sim 10^9$ cm$^{-3}$ in the corona to $\gtrsim 10^{11}$ cm$^{-3}$ in the chromosphere [58, 59]. Due to the low plasma density in the corona, the mean free path of energetic electrons is large, and such particles travel along this leg of the path following the reconnected magnetic field lines with virtually no Coulomb energy losses (such that the energy spectrum of electrons can be considered unchanged). Even relatively rare collisions lead to the generation of hard X-ray bremsstrahlung in the corona, which is described well by the classical thin-target model (see review [12]).

Penetrating into the chromosphere, where the plasma density is much higher ($\gtrsim 10^{11}$ cm$^{-3}$), electrons rapidly lose their kinetic energy due to Coulomb collisions. Here, as in the corona, they generate hard X-rays, and quite often the most intense ones [12, 50]. The sources of this radiation are located at the bases of the so-called 'flare loops' — tubes of reconnected magnetic field lines; the totality of the tube bases form 'flare ribbons,' which are accessible to the most comprehensive study with the help of ground and space observations [33].

To describe the evolution of the distribution function of energetic particles during their propagation in the chromosphere, a simplified thick-target model [60] is widely used, wherein the effect of collisional scattering of beam electrons is taken into account approximately. As a consequence of the simplification, the applicability range of the model is limited

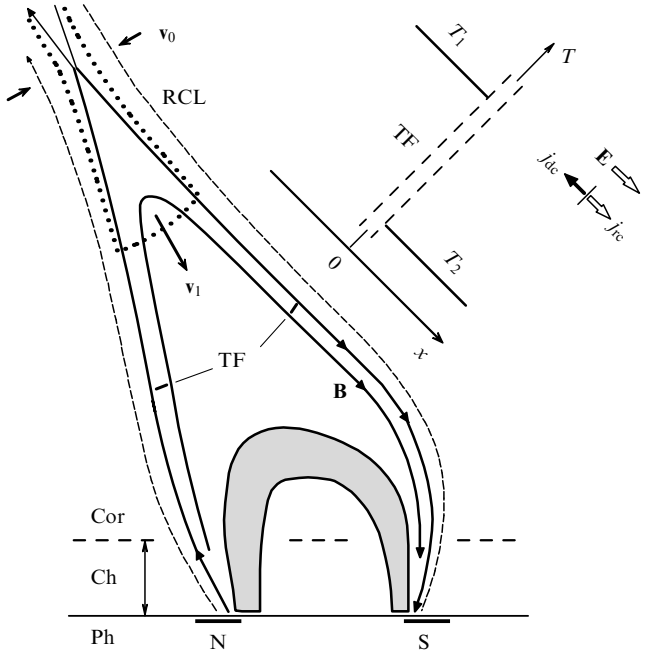


**Figure 1.** Most significant part of the classical picture of a solar flare. Electrons accelerated in the reconnecting current layer RCL escape from the superhot plasma with temperature $T_1$ through the turbulent front TF into the colder target plasma with temperature $T_2$.

to small depths of electron penetration into the target (see Section 2.3 for details). As regards interpreting observations, the classical model of Syrovatskii and Shmeleva [61] is more suitable, as it accurately takes collisions into account based on an analytic solution of the corresponding kinetic equation with the Landau collision integral.

The first kinetic models (which we here refer to as classical) did not have the merit of high accuracy, but they allowed a qualitative understanding of the physical nature of the individual processes that make up the observed pattern of solar flares. The classical models ideally corresponded to the accuracy of observations of the time and provided reasonable answers to the questions that confronted the theory of solar flares in the 1970s.

As regards modern observations of solar flares (primarily powerful flares), such models face significant difficulties [62]. One of the problems is that the classical models do not take the reverse current effect into account, although its existence seems obvious. Indeed, a large number of charged particles [63] precipitate from the acceleration region into the solar corona and the chromosphere, creating an electric current $j_{dc} \gtrsim 10^{17}$ A. However, the magnetic fields corresponding to these currents ($B_0 \gtrsim 10^5$ G) is not observed in solar flares [34, 64]. This is due to the appearance of electrostatic and inductive electric fields in the plasma of the solar atmosphere; the effect of these fields is that thermal particles create a reverse current that compensates the direct current. With the sign of the electron charge taken into account, in Fig. 1 we show the directions of the direct ($j_{dc}$) and reverse ($j_{rc}$) currents, together with the electric field strength **E** of the reverse current. Of course, the total electric field also acts on the beam electrons, significantly altering their propagation pattern.

The next-generation models [65, 66] superseding the classical thick- and thin-target models take the electric field of the reverse current into account. These models can be called

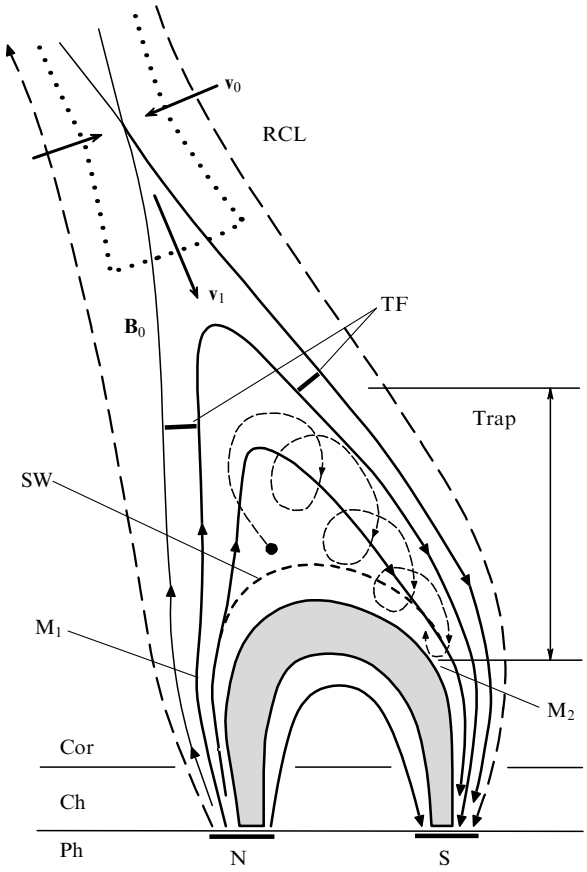


**Figure 2.** Diagram of a solar flare with a magnetic trap. RCL — reconnecting current layer, primary source of accelerated electrons; SW — shock wave over a 'magnetic obstacle'; Trap — a collapsing magnetic trap in the corona between the turbulent front TF and magnetic mirrors $M_1$ and $M_2$. Dotted spiral conventionally shows the trajectory of an electron captured in a trap.

'neoclassical.' Their principal feature and great advantage is that they are two-dimensional in terms of the velocity space (see [28, Ch. 4]).

However, we here face another problem that was not foreseen in either classical or neoclassical models: how to explain the observed intensity of hard X-rays in the corona? The problem can be solved because the ratio of the intensities of the coronal and chromospheric radiation sources and their temporal and spectral features depend on the efficiency of betatron heating and first-order Fermi acceleration inside flare loops, which play the role of so-called *collapsing* magnetic traps [67].

As noted above, electrons in solar flares are first accelerated by the electric field in a reconnecting current layer (see Fig. 1). After this first step in the accelerating process, they enter coronal magnetic traps (Fig. 2), whose length along the magnetic field lines and the transverse size (thickness) rapidly decrease [67]. In such collapsing traps, the trapped electrons are reflected either from a shock wave located on the trajectory of a high-speed plasma flow emanating from the current layer or from magnetic mirrors $M_1$ and $M_2$ (see Fig. 2). In the case of relatively slow magnetic reconnection, the shock wave may not arise, and reflection then occurs solely on the magnetic mirrors $M_1$ and $M_2$ [29]. Inside a collapsing trap, electrons acquire additional acceleration via the first-order Fermi mechanism and betatron heating.

An additional, or secondary, increase in the energy of electrons is of fundamental importance for the correct interpretation of modern observations of solar flares: taking the primary acceleration in the reconnecting current layer into account is insufficient in some flares (see, e.g., [30, Section 3.3.2]). The scenario of additional acceleration of electrons of one population (acceleration in the current layer followed by acceleration of the same electrons in a collapsing magnetic trap), proposed in [67] and called the *double step* acceleration, has not yet been confirmed by reliable observations of flares and therefore remains largely a theoretical prediction. This effect should not be confused with so-called two-phase acceleration, when the electrons initially accelerated during the impulsive phase of the flare (several seconds or tens of seconds) are accelerated to relativistic energies (as was previously assumed, on shock waves) much later, during the second phase of the flare, delayed by several minutes to several hours [68].

Such is the outline of the modern picture of a solar flares. Its interpretation remains one of the main problems in solar physics. In view of progress in space observations of the Sun, the classical kinetic models [61] and especially the 'simplified classical models' [60, 69, 70] either do not provide the required accuracy or are not applicable to interpreting some events [62, 71, 72]. In modern numerical models of solar flares [30, 31, 73], the kinetic problem of the propagation of accelerated particles in the flares is considered in a sufficiently general formulation, but a large number of model parameters, together with high computation costs, complicate the understanding of the main physical processes and of the role they play in solar flares.

### 2.2 Setting up the problem of energetic runaway electrons

In astrophysical plasma in general and in solar flares in particular, electron acceleration is always accompanied by plasma heating, and vice versa, plasma heating gives rise to energetic electrons escaping from it [28]. During flares, as noted, the magnetic field energy is converted in current layers into thermal and kinetic energy of plasma and accelerated particles. The accelerated particles then excite plasma turbulence, which heats the electron component of the plasma in the layer to enormous temperatures $T_e \gtrsim 10^8$ K [74]. Such a layer is known as a *superhot* turbulent current layer [29].

Heat fluxes, in the form of huge-amplitude thermal waves, and streams of accelerated particles very rapidly propagate from the current layer along reconnected magnetic field lines. The magnetic field lines form bright magnetic field tubes, called flare loops (see Fig. 1.2.6 in [13]). At temperatures $T_e \gtrsim 10^6$ K in solar flares, the thermal wave front is highly turbulent, and the classical electron heat conduction along the magnetic field is suppressed. However, similarly to the usual thermal runaway effect for electrons associated with Coulomb collisions in plasma in the presence of a large temperature gradient (see [28, §8.4.3]), the electrons with speeds exceeding some critical speed $v_{cr}$ [75] penetrate almost freely through the turbulent layer from a superhot ($T_1 \gtrsim 10^8$ K) plasma into a much colder plasma: $T_2 \gtrsim 10^6$ K in the corona and $T_2 \lesssim 10^4$ K in the chromosphere. Electrons with lower speeds stay in the superhot source.

We consider the general problem setup for energetic runaway electrons that penetrate through a turbulent front and propagate in a cold plasma (see Fig. 1). For simplicity, we let the superhot and cold plasma respectively occupy two half-

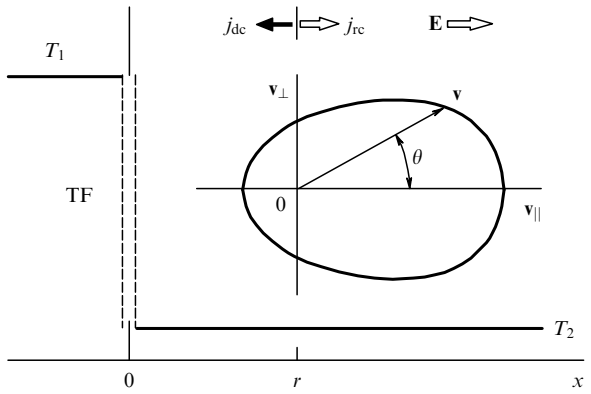


**Figure 3.** Setting up the problem of energetic electrons that escaped from a superhot plasma with a temperature $T_1$ through a turbulent front TF into a colder plasma with a temperature $T_2$. $r$ is the distance from the turbulent front to the point at which the electron distribution function is considered; **E** is the reverse-current electric field strength; $\mathbf{v}_\perp$ and $\mathbf{v}_\parallel$ are the transverse and longitudinal components of electron velocity vector **v**.

spaces $x < 0$ and $x > 0$, separated by a flat thin turbulent layer at $x = 0$ (Fig. 3). We also assume, unless stipulated otherwise, that the magnetic field is uniform and directed along the $x$-axis, i.e., perpendicular to the interface of superhot and cold plasmas.

Let the distribution function of energetic electrons in the source $f_{\mathbf{vs}}$ be axially symmetric with respect to the magnetic field direction. Then, the boundary distribution function of electrons flying forward into the cold target plasma is

$$f_{\mathbf{vff}}(0, v, \theta) = f_{\mathbf{vs}}(v, \theta)\, \Theta(v - v_{\min})\, \Theta(v_{\max} - v)\,. \qquad (1)$$

Here, $v$ is the electron speed, $\theta$ is the angle between the velocity vector **v** and the magnetic field direction, $v_{\min}$ and $v_{\max}$ are the minimum and maximum electron speeds, and the theta function is defined as $\Theta(x) = 1$ for $x \geqslant 0$ and $\Theta(x) = 0$ for $x < 0$. The subscript **v** indicates that the sought function $f_{\mathbf{v}} = f_{\mathbf{v}}(r, v, \theta)$ is the distribution function of electrons along the velocity vector **v**. The expected form of this function at a distance $r$ from the turbulent front is conventionally shown in the two-dimensional velocity space in Fig. 3.

We discuss the choice of the normalization condition for such a distribution function separately. From the standpoint of interpreting observations of solar flares in hard X-rays, the energy flux density $F$ at the target boundary, carried by energetic electrons injected through the turbulent front, is an essential physical parameter of the problem, needed when calculating the processes occurring in the target. Indeed, $F$ takes various characteristics of the injection spectrum into account: the concentration of energetic electrons, their minimum and maximum energies, and the slope. When modeling a flare, the inverse problem is to be solved: the energy flux $F$ is to be reconstructed from the observed intensity of hard X-ray radiation at the bases of flare loops. The electron distribution function is then normalized to the intensity as follows:

$$F\ [\text{erg cm}^{-2}\ \text{s}^{-1}] = \int f_{\mathbf{v}}(0, v, \theta)\, v \cos\theta\, \frac{mv^2}{2}\, \mathrm{d}\mathbf{v}\,. \qquad (2)$$

The observed hard X-ray emission in both the corona and the chromosphere consists of two components, nonthermal and thermal. The nonthermal component is due to brems-

strahlung from accelerated electrons, and the thermal component is due to bremsstrahlung from heated plasma electrons. Near the lower boundary of the energy spectrum of accelerated electrons, Coulomb collisions can play a role. They lead to the Maxwellianization of electrons and hence to thermal hard X-ray radiation. The spectra of nonthermal and thermal hard X-ray radiation partially overlap.

In the general case, the distribution function $f_{\rm vs}$ of electrons in the source, i.e., in a reconnecting superhot turbulent current layer and in the plasma flowing out of it, consists of two parts, thermal and nonthermal. The first describes superhot electrons and is usually assumed to have the Maxwellian form [65]. The second part corresponds to accelerated electrons and is a power-law function [66].

Forward-flying energetic electrons, both thermal and nonthermal, carry an electric current, standardly called the *direct* current, which is by definition equal to

$$j_{\rm dc}(r) = e\int f_{\mathbf{v}}\,(r, v, \theta)\, v\,\cos\theta\,\mathrm{d}\mathbf{v}\,. \tag{3}$$

Taking the sign of the electron charge into account, the direct current flows backwards, toward the turbulent front, as shown in Fig. 3.

It can be reasonably assumed that the direct current is completely balanced in the solar flare plasma by the *reverse* current $j_{\rm rc}$:

$$|\,j_{\rm dc}\,(r)\,| = j_{\rm rc}\,(r) \equiv j\,(r)\,. \tag{4}$$

This means that a very fast process of reverse current generation has enough time to balance the direct current in a time comparable to the period of plasma oscillations, which, under the conditions considered here, is much shorter than the Coulomb collision time [76]. In addition, we ignore any high-frequency changes in the distribution function of accelerated electrons in the plasma and therefore also ignore any high-frequency electric fields that require taking the displacement current in Maxwell's equations into account.

As regards thermal electrons in a cold plasma, we assume that they are the source of resistance to the reverse current, unchanged with time. That is, we assume that the stationary electric field $E = E\,(r)$ that causes the reverse current and decelerates forward-flying energetic electrons (see Fig. 3) can be found simply from Ohm's law,

$$E\,(r) = \frac{j\,(r)}{\sigma}\,, \tag{5}$$

where $\sigma$ is the plasma conductivity, which is determined exclusively by Coulomb collisions. In other words, we assume that the speed of reverse-current electrons is not high enough to excite turbulence outside the turbulent front. We note that the reverse current is mainly produced by electrons of the colder target plasma. They can acquire speeds sufficient to overcome the turbulent front, penetrate into the acceleration region, and accelerate further. It was shown in [77] that the effect can be significant and must be taken into account in a self-consistent manner when constructing flare models. Among the particles flying backwards (toward the turbulent front), there is also a second group made of the accelerated electrons of the beam that turned back under the action of the electric field of the reverse current.

We describe the behavior of the distribution function of energetic electrons in the target by the kinetic equation [28]

$$v\cos\theta\,\frac{\partial f_{\mathbf{v}}}{\partial x} - \frac{eE}{m_{\rm e}}\cos\theta\,\frac{\partial f_{\mathbf{v}}}{\partial v} - \frac{eE}{m_{\rm e}v}\sin^2\theta\,\frac{\partial f_{\mathbf{v}}}{\partial\cos\theta} = \mathrm{St}_{\rm L}\,(f_{\mathbf{v}})\,. \tag{6}$$

It is taken into account here that, at times of the order of the Coulomb collision time in the cold plasma of the target, the process of electron injection can be considered stationary, and their distribution in the target, in the half-space $x > 0$ (see Fig. 3), can be considered steady. In the kinetic equation, we therefore set the derivative $\partial/\partial t$ equal to zero. The second and third summands express the term

$$\frac{(-e)}{m_{\rm e}}\,\mathbf{E}\,(\mathbf{r})\,\frac{\partial f_{\mathbf{v}}}{\partial\mathbf{v}}$$

in the $v$ and $\theta$ variables. In addition, as was assumed above, the distribution function is axially symmetric and therefore the term with the magnetic field on the left-hand side of the kinetic equation vanishes (see [28, Section 4.1.1]).

We also assume that the cold plasma consists of electrons and protons that have a constant temperature $T_2$. Of course, both electrons and protons contribute to the right-hand side of Eqn (6), which is chosen in the form of the Landau collision integral

$$\mathrm{St}_{\rm L}\,(f_{\mathbf{v}}) = \frac{1}{v^2}\,\frac{\partial}{\partial v}\left[v^2\nu_{\rm coll}(v)\left(\frac{k_{\rm B}T_2}{m_{\rm e}}\,\frac{\partial f_{\mathbf{v}}}{\partial v} + v f_{\mathbf{v}}\right)\right] + \nu_{\rm coll}\,(v)\,\frac{\partial}{\partial\,\cos\theta}\left(\sin^2\theta\,\frac{\partial f_{\mathbf{v}}}{\partial\cos\theta}\right). \tag{7}$$

It is understood in (7) that the kinetic energy of superhot and accelerated electrons is much greater than the energy of thermal electrons in the colder target plasma. The linearized Landau collision integral can therefore be used, with the rate of collisions of energetic electrons with thermal electrons and protons in the plasma given by

$$\nu_{\rm coll}(v) = \frac{4\pi\,n_2 e^4}{m_{\rm e}^2\,v^3}\,\ln\Lambda\,, \tag{8}$$

where $n_2$ is the electron concentration in the cold plasma and $\ln\Lambda$ is the Coulomb logarithm.

It is convenient to introduce the dimensionless variables and parameters as follows: $\mu = \cos\theta$;

$$s = \frac{\pi e^4\ln\Lambda}{(k_{\rm B}T_1)^2}\int_0^r n_2(x)\,\mathrm{d}x$$

is the ratio of the penetration depth of energetic electrons into the target to the mean free path of thermal electrons in the superhot plasma;

$$z = \frac{m_{\rm e}v^2}{2k_{\rm B}T_1}$$

is the ratio of the kinetic energy of energetic electrons to the thermal energy of superhot plasma particles; $\tau = T_2/T_1$ is the ratio of the cold to superhot plasma temperatures; and

$$\varepsilon = \frac{k_{\rm B}T_1 E}{2\pi\,n_2\,e^3\ln\Lambda}$$

is the ratio of the reverse-current electric field strength to the Dreiser field strength in the cold plasma.

The unknown function $E = E(s)$ must be found from a self-consistent solution to the kinetic problem, i.e., a common solution of Eqn (5) and (6). In the new variables, kinetic equation (6) becomes

$$\mu z^2 \frac{\partial f_{\mathbf{v}}}{\partial s} - 2\varepsilon\mu z^2 \frac{\partial f_{\mathbf{v}}}{\partial z} - \varepsilon z (1-\mu^2) \frac{\partial f_{\mathbf{v}}}{\partial \mu} = 2z \frac{\partial f_{\mathbf{v}}}{\partial z} + 2\tau z \frac{\partial^2 f_{\mathbf{v}}}{\partial z^2} + \frac{\partial}{\partial \mu}\left[(1-\mu^2) \frac{\partial f_{\mathbf{v}}}{\partial \mu}\right]. \quad (9)$$

Because we are primarily interested in the electrons accelerated in the reconnecting current layer, we take only the power-law part of the electron distribution function at the target boundary:

$$f_{\mathrm{vff}}(0, z, \mu) = K z^{-\gamma_{\mathbf{v}}} \Theta(z - z_{\min}) \Theta(z_{\max} - z). \quad (10)$$

Here, the dimensionless energies $z_{\min}$ and $z_{\max}$ correspond to the lower and upper bounds of the energy spectrum of accelerated electrons. The constant $K$ is determined from normalization condition (2) and, taking condition (10) into account, has the form

$$K = \begin{cases} F(3-\gamma_{\mathbf{v}}) \left[\dfrac{2\pi (k_{\mathrm{B}} T_1)^3}{m_{\mathrm{e}}^2} \left(z_{\max}{}^{3-\gamma_{\mathbf{v}}} - z_{\min}{}^{3-\gamma_{\mathbf{v}}}\right)\right]^{-1}, & \gamma_{\mathbf{v}} \neq 3, \\ F \left[\dfrac{2\pi (k_{\mathrm{B}} T_1)^3}{m_{\mathrm{e}}^2} \ln\left(\dfrac{z_{\max}}{z_{\min}}\right)\right]^{-1}, & \gamma_{\mathbf{v}} = 3. \end{cases} \quad (11)$$

Let us recall that, in Eqn (9) and everywhere below, the function $f_{\mathbf{v}}(s, z, \mu)$ is still the distribution function of accelerated electrons along the velocity vector $\mathbf{v}$, with a simple change of variables, from the velocity vector modulus $v$ to the corresponding dimensionless kinetic energy $z$. In dimensionless variables, the problem naturally remains two-dimensional in the velocity space, which is of fundamental importance.

Kinetic equation (9) under the boundary condition given in (10) uniquely determines the evolution of the stream of accelerated electrons in the target and hence the characteristics of the radiation generated by them. The following model parameters must then be specified: the superhot and cold plasma temperatures $T_1$ and $T_2$, and the cold plasma density $n_2$. Numerical values of these parameters can be estimated with a certain accuracy based on the results of observations [78]. In addition, observations of the spectrum of hard X-ray radiation are used to select the characteristics of accelerated electrons such as the energy flux density $F$ and the exponent of the injection spectrum slope $\gamma_{\mathbf{v}}$.

### 2.3 Classical thin- and thick-target models

Ignoring the energy diffusion and the reverse-current electric field, i.e., setting $\varepsilon(s) = 0$ in kinetic equation (9), we write it in the classical limit in the form

$$\mu z^2 \frac{\partial f_{\mathbf{v}}}{\partial s} = 2z \frac{\partial f_{\mathbf{v}}}{\partial z} + \frac{\partial}{\partial \mu}\left[(1-\mu^2) \frac{\partial f_{\mathbf{v}}}{\partial \mu}\right]. \quad (12)$$

Here, regular energy losses and changes in the angular distribution (angular diffusion) of energetic electrons due to their Coulomb collisions with thermal plasma particles during propagation in the solar atmosphere are taken into account.

If the term that describes the angular diffusion of accelerated electrons is disregarded on the right-hand side of (12), the equation becomes the kinetic equation in the form considered when constructing the classical thin- and thick-target models [61],

$$\mu \frac{\partial f_{\mathbf{v}}}{\partial s} = \frac{2}{z} \frac{\partial f_{\mathbf{v}}}{\partial z}, \quad (13)$$

where $\mu = \text{const}$ because scattering is absent.

Equation (13) with boundary condition (10) has a well-known and frequently used analytic solution ($\mu = 1$)

$$f_{\mathbf{v}}(z, s) = K (z^2 + 2s)^{-\gamma_{\mathbf{v}}/2} \Theta(z - z'_{\min}) \Theta(z'_{\max} - z), \quad (14)$$

where

$$z'_{\min,\max} = \mathrm{Re}\,(z^2_{\min,\max} - 2s)^{1/2}.$$

A similar solution was obtained in [60] and is being used equally frequently in interpreting X-ray emission in the chromosphere. However, in comparison with (14), it is less accurate, because the author took collisions of energetic electrons with background plasma particles into account only approximately.

Let us comment on the role of angular electron diffusion in problem (12). As noted above, the effect is due to a change in the direction of electron motion during electron Coulomb collisions with plasma particles and is not small (see [28, Section 4.2]). But neither classical solution (14) nor the solution obtained in [60] take it into account, even though angular diffusion leads to a significant limitation of the beam penetration depth into the target compared to the classical thick-target models (see [28, Section 4.4]). This is why these models predict incorrect electron bremsstrahlung characteristics, including overestimated polarization values [79]. The evolution of an electron beam in the solar atmosphere is most accurately described by Eqn (9), whose analytic solution is considered in Section 3.2.

We nevertheless use solution (14) as a standard in interpreting hard X-ray radiation in the chromosphere, i.e., in a thick target. The physical meaning of this solution is easy to understand: accelerated electrons propagating along the supposedly uniform magnetic field in the absence of angular diffusion do not change their angular distribution, and their energy spectrum shifts due to Coulomb collisions to lower energies, becoming harder.

In the approximation of the classical thin-target model ([69], also see [12, 61]), which is used to describe motion in thin plasma layers, the distribution function and hence the spectrum of accelerated electrons change insignificantly. This approximation is suitable for interpreting hard X-ray radiation in the corona, where the background plasma density is relatively low, and is used in this paper to interpret coronal sources of hard X-rays produced by flares. The formalism of the thin-target model used here is taken from [12].

### 2.4 Kinetic equation for high-energy electrons

For a more complete description of the existing variety of kinetic models of solar flares, we consider one more limit case, the propagation of accelerated electrons in the solar atmosphere with a conventional lower energy bound (for example, $\mathcal{E} \gtrsim 120$ keV) in an *inhomogeneous* magnetic field that increases toward the flare loop bases.

Recall that in [61], in calculating the hard X-ray emission of accelerated electrons in specific solar flares, the upper

bound of their energy spectrum was conventionally assumed to be infinitely large. This is justified. Even for powerful flares with a very hard injection spectrum, the slope exponent is $\gamma_{\mathbf{v}} \geqslant 2$, and hence estimates of the hard X-ray flux density are almost independent of the choice of a sufficiently large upper bound of the spectrum. Indeed, such particles not only are relatively few among the injected electrons but also experience no significant energy losses in Coulomb collisions or in the reverse-current electric field. Nevertheless, such electrons [80, 81] make the dominant contribution to the high-frequency part ($\gtrsim 10$ GHz) of the gyrosynchrotron radio spectrum.

In [70], in the case where the energy of accelerated electrons is so high that Coulomb collisions and the influence of the reverse-current electric field can be ignored, an analytic solution was obtained for the simple kinetic equation

$$\frac{\partial f_{\mathbf{v}}}{\partial s} = \frac{1-\mu^2}{2}\,\alpha_B\,\frac{\partial f_{\mathbf{v}}}{\partial \mu}\,, \tag{15}$$

which includes only the magnetic field (more precisely, its inhomogeneity; cf. Eqn (6), which takes everything else into account). Here, $\alpha_B(s) = \ln\left(B(s)/B(0)\right)$ is the logarithm of the ratio of the magnetic field at the flare loop bases to the field at its top.

Equation (15) is solved by

$$f_{\mathbf{v}}(s,z,\mu) = f_{\mathbf{v}0}\left(z, \left[1-(1-\mu^2)\exp\left(\alpha_B(s)\right)\right]^{1/2}\right), \tag{16}$$

where $f_{\mathbf{v}0}$ is the boundary electron distribution function. Formula (16) describes a simple and natural behavior pattern of high-energy particles (with negligibly small energy and scattering losses) trapped in a magnetic trap (see Section 3.3). In principle, analytic solutions (14) and (16) allow obtaining a model description of the propagation of electrons of the entire energy spectrum in the classical approximation, i.e., without taking reverse currents and collapsing magnetic traps into account.

### 2.5 Thermal runaway electrons in solar flares

In addition to accelerated electrons, thermal electrons with speeds $v > v_{\mathrm{cr}}$ can also propagate from a superhot source through the turbulent front (see Fig. 1) into the colder plasma of the corona and the chromosphere. A model description of their propagation is of great practical importance, because such particles generate X-ray bremsstrahlung with photon energies $\mathcal{E}_{h\nu} \sim 10$–$20$ keV (the thermal component in the spectra of coronal and chromospheric sources), whose spectrum and polarization can be explored with the existing and future space observatories. Of course, without taking this spectral component into account, the interpretation of X-ray observations of solar flares (especially polarization observations) cannot be complete.

The problem of the propagation of thermal runaway electrons during solar flares was considered in detail in [82], where the authors found an analytic solution of a kinetic equation that can be obtained from Eqn (9). Ignoring the reverse-current electric field $\varepsilon$, we have

$$z^2\mu\,\frac{\partial\varphi}{\partial s} - 2z\,\frac{\partial\varphi}{\partial z}\left(1-\tau\,\frac{\partial\varphi}{\partial z}\right) - 2\tau z\,\frac{\partial^2\varphi}{\partial z^2} + 2\mu\,\frac{\partial\varphi}{\partial\mu} + (1-\mu^2)\left(\frac{\partial\varphi}{\partial\mu}\right)^2 - (1-\mu^2)\left(\frac{\partial^2\varphi}{\partial\mu^2}\right) = 0\,. \tag{17}$$

Instead of the distribution function $f_{\mathbf{v}}$, we here introduce the new function

$$\varphi = -\ln f_{\mathbf{v}}\,, \tag{18}$$

which is convenient when considering distribution functions that differ only a little from the Maxwellian one. The approximate analytic solution of this kinetic problem obtained in [82] has the form

$$f_{\mathbf{v}}(z,\mu,s) = K\begin{cases} \exp\left[-\left(z+2\,\dfrac{s}{z}\right)\right], & \mu > \left(\dfrac{s}{z}\right)^2, \\ & s < a\,,\ z > s^{1/2}; \\ \exp\left[-\left(z+2\,\dfrac{s}{z}\,(2-\mu)+\dfrac{s}{z}\,(1-\mu)^2\right)\right], & \mu \gtrsim \dfrac{s}{(s^{1/2}+1)^2}, \\ & s > a\,,\ z > s^{1/2}; \\ \exp\left[-(z+2s^{1/2})\right], & z < s^{1/2}\,. \end{cases} \tag{19}$$

The parameter $a$ is needed to ensure the matching of the first two distributions in (19). The choice of this parameter somewhat affects the degree of anisotropy of superhot electrons and hence the polarization of their bremsstrahlung, but as shown in [82], this influence manifests itself only at energies so high that the hard X-ray flux is negligible from the standpoint of the practical options of polarization measurements. We discuss this in Section 4.

We note that solution (19) is applicable in those cases where thermal electrons have much higher energies than the energies of particles in the colder surrounding plasma of the corona and the chromosphere. In other words, energy diffusion can be disregarded in (17). Where the energy of electrons $z \to 1$, energy diffusion must be taken into account, which fundamentally changes the evolution of their distribution function [83].

## 3. Modern models of electron propagation and additional acceleration in solar flares

### 3.1 Some simplifying assumptions

From a mathematical standpoint, the kinetic problem posed in Section 2.2, Eqn (9), is a system of integrodifferential equations for two unknown functions $f_{\mathbf{v}}(s,z,\mu)$ and $\varepsilon(s)$. Equation (9) is a complex partial differential equation, solving which, even with a given function $\varepsilon(s)$, is quite difficult. However, this equation allows considerable simplifications if we recall that the dimensionless parameters involved in it are small in the conditions of solar flares.

The first such parameter is $\tau \sim 10^{-1}$–$10^{-4}$, in view of the huge temperature $T_1$ in the superhot source of accelerated electrons. This allows the term with the second derivative with respect to the dimensionless energy $z$ to be ignored, i.e., ignoring energy diffusion in the kinetic equation.

Before discussing the second dimensionless parameter, $\varepsilon$, we note a fundamental property of the problem under consideration. For this, after setting $\tau = 0$, we divide the resultant equation by $z$ and integrate it over $z$ and $\mu$. Using the definition of direct current (3) rewritten in dimensionless variables, we verify that only one term, $z\,(\partial f_{\mathbf{v}}/\partial z)$, on the right-hand side of the original equation (9), makes a nonzero

contribution to the equation for the behavior of the direct current in the target [65],

$$\frac{\mathrm{d}j}{\mathrm{d}s} = -a_1 \int_{-1}^{1} f_{\mathrm{v}}(0, s, \mu)\,\mathrm{d}\mu\,, \tag{20}$$

where the constant is $a_1 = \pi e\,(2k_{\mathrm{B}}T_1/m_{\mathrm{e}})^2$. The integral on the right-hand side of (20) is greater than zero. Indeed, it expresses the number of electrons at a depth $s$ that have lost their kinetic energy due to Coulomb collisions while moving in the target. Their number is evidently nonzero, and therefore the electric current of the flux of accelerated electrons decreases as it penetrates the target exclusively due to the Coulomb energy losses. If collisions were absent, the current would not change. Relatively rare collisions of energetic electrons (regardless of their nature) with thermal electrons of cold plasma play a key role in the self-consistent reverse-current problem.

We turn to the second dimensionless parameter. Because electrons accelerated in solar flares create huge currents [63, 84], it is natural to assume in view of (5) that the reverse-current electric field $\varepsilon$ is also very large, and hence the energy losses caused by the electric field and the change in the angular distribution of electrons are much higher than they would have been in the case of only Coulomb collisions. Hence, the following inequalities hold:

$$2\varepsilon\mu z^2\,\frac{\partial f_{\mathrm{v}}}{\partial z} \gg 2z\,\frac{\partial f_{\mathrm{v}}}{\partial z}\,, \tag{21}$$

$$\varepsilon z\,(1-\mu^2)\,\frac{\partial f_{\mathrm{v}}}{\partial \mu} \gg \frac{\partial}{\partial \mu}\left[(1-\mu^2)\,\frac{\partial f_{\mathrm{v}}}{\partial \mu}\right]. \tag{22}$$

Taking (22) into account, we can disregard the angular diffusion on the right-hand side of (9) and keep only the term describing the regular energy losses in Coulomb collisions.

Despite the validity of condition (21), the term $2z\,(\partial f_{\mathrm{v}}/\partial z)$, which describes regular energy losses due to Coulomb collisions, cannot be ignored on the right-hand side of Eqn (9), because that would imply the limit of collisionless plasma. Then, as it should be in a collisionless plasma, $\mathrm{d}j/\mathrm{d}s = 0$ and hence $j(s) = \mathrm{const}$, which means either that the current vanishes everywhere in the target once it is equal to zero at infinity or that its value is conserved wherever the collisionless approximation is applicable. Near the target boundary, where the reverse-current electric field is very strong, condition (21) is valid, and, given the low collision rate, the current indeed remains nearly constant.

Here, we also disregard thermal and hydrodynamic phenomena associated with the heating of a cold target plasma by electrons of direct and reverse currents [85] (see, however, [13, § 2.1.7]).

### 3.2 Self-consistent analytic thick-target model with reverse current

**3.2.1 Reverse-current electric field.** We introduce a new variable, the dimensionless potential of the reverse-current electric field

$$\phi = \int_0^s \varepsilon\,(s')\,\mathrm{d}s'\,.$$

Using Ohm's law (5), also written in dimensionless form

$$\varepsilon = b_1 j\,,$$

where

$$b_1 = \frac{k_{\mathrm{B}}T_1}{2\pi e^3 n_2\,\sigma \ln \Lambda}\,,$$

we use Eqns (9) and (20) to obtain the system of integrodifferential equations

$$\frac{\partial f_{\mathrm{v}}}{\partial \phi} - \left[2 + \frac{2}{\varepsilon(\phi)\,\mu z}\right]\frac{\partial f_{\mathrm{v}}}{\partial z} - \frac{1}{z}\,\frac{1-\mu^2}{\mu}\,\frac{\partial f_{\mathrm{v}}}{\partial \mu} = 0\,, \tag{23}$$

$$\frac{\mathrm{d}\varepsilon^2}{\mathrm{d}\phi} = -2a_1 b_1 \int_{-1}^{+1} f_{\mathrm{v}}(0, \mu, \phi)\,\mathrm{d}\mu\,. \tag{24}$$

We supplement Eqn (23) with boundary condition (10), where $\mu > 0$.

To solve this complicated problem, we use the classical method of characteristics (see [86, § 3.3]). We seek a solution in the form

$$f_{\mathrm{v}}(z, \mu, \phi) = f_{\mathrm{v}0}(X, Y)\,, \tag{25}$$

where $X$ and $Y$ are to be found from the system of ordinary differential equations for characteristics,

$$\begin{aligned} &\frac{\mathrm{d}z}{\mathrm{d}\phi} = -2 - \frac{2}{\varepsilon\mu z}\,, \quad z(0) = X\,,\\ &\frac{\mathrm{d}\mu}{\mathrm{d}\phi} = -\frac{1-\mu^2}{\mu z}\,, \quad \mu(0) = Y\,. \end{aligned} \tag{26}$$

In general, this system of equations can be solved analytically, but only in implicit form. However, using condition (21) in the form $\varepsilon \gg \mu z$, we find an approximate explicit solution:

$$\begin{aligned} &X = z + 2\phi\,,\\ &Y = \operatorname{sign}\mu\left(\mu^2 + \frac{2\phi}{z}\right)^{1/2}\left(1 + \frac{2\phi}{z}\right)^{-1/2}. \end{aligned} \tag{27}$$

Here, $\operatorname{sign}\mu = -1$ if $\mu < 0$ and $\operatorname{sign}\mu = 1$ if $\mu \geqslant 0$.

We use the obtained solution to write an expression for the function $\varepsilon(\phi)$. From Eqn (25), we obtain

$$f_{\mathrm{v}}(0, \mu, \phi) = K(2\phi)^{-\gamma_{\mathrm{v}}}\,\Theta(2\phi - z_{\min})\,.$$

With (24), we therefore have

$$\begin{aligned} \frac{\mathrm{d}\varepsilon^2}{\mathrm{d}\phi} &= -2a_1 b_1 \int_{-1}^{1} f_{\mathrm{v}}(0, \mu, \phi)\,\mathrm{d}\mu\\ &= -4a_1 b_1 K(2\phi)^{-\gamma_{\mathrm{v}}}\,\Theta(2\phi - z_{\min})\,. \end{aligned} \tag{28}$$

Integrating over $\phi$, we find the sought function

$$\varepsilon(\phi) = \begin{cases} \left(\dfrac{2a_1 b_1 K}{\gamma_{\mathrm{v}} - 1}\right)^{1/2}(2\phi_0)^{(1-\gamma_{\mathrm{v}})/2} = \varepsilon_0 = \mathrm{const}, & \phi < \phi_0 = \dfrac{z_{\min}}{2},\\ \left(\dfrac{2a_1 b_1 K}{\gamma_{\mathrm{v}} - 1}\right)^{1/2}(2\phi)^{(1-\gamma_{\mathrm{v}})/2}, & \phi > \phi_0\,. \end{cases} \tag{29}$$

Thus, according to the approximate solution, the electric field of the reverse current in the target is constant through the depth $\phi_0$ and rapidly decreases at greater depths.

For simplicity, approximate solution (29) was obtained under the condition $z_{\max} \to \infty$, which, as noted in Section 2.4, is quite justified. We note one more natural bound: the energy

$z_{cr}$ of electrons capable of overcoming the turbulent front (TF in Fig. 3) that separates superhot, hot, and colder plasmas. The threshold electron runaway velocity $v_{cr}$ is determined by the approximate formula [75]

$$v_{cr} \approx 2.8\left(\frac{k_B T_l}{m_e}\right)^{1/2}, \tag{30}$$

which corresponds to the excitation of ion–acoustic waves by the reverse current inside the turbulent front. Consequently, boundary distribution function (10) describes the electrons with a speed greater than the speed in (30), which means that the minimum energy of electrons penetrating through the turbulent front is $z_{min} \geqslant z_{cr}$.

**3.2.2 Distribution function of energetic electrons.** To find the distribution function of accelerated electrons in the target, instead of approximate solution (27), we use a more accurate solution of the system of characteristic equations proposed in [65] for runaway superhot electrons:

$$X = z + \frac{1}{\varepsilon}\left(\ln\frac{1+Y}{1-Y} - \ln\frac{1+\mu}{1-\mu}\right) + 2\phi\,, \tag{31}$$

$$Y = \operatorname{sign}\mu\left(\mu^2 + \frac{2\phi}{z}\right)^{1/2}\left(1+\frac{2\phi}{z}\right)^{-1/2}. \tag{32}$$

We note that, for electrons flying backwards, i.e., returning to the source, the distribution function $f_{v\,bf}$ is not fixed at the boundary (cf. (10)), but must be found from a self-consistent solution to the problem. Naturally, this corresponds to the fact that, in the method of characteristics, the boundary conditions are imposed on the incoming characteristics. Using the boundary distribution function of electrons flying forward, Eqn (10), we use (31) and (32) to first find the boundary distribution function of backward electrons,

$$f_{v\,bf} = K\left(z + \frac{2}{\varepsilon\,(z\mu^2/2)}\ln\frac{1-\mu}{1+\mu}\right)^{-\gamma_v}\Theta(-\mu)\,. \tag{33}$$

Next, with (31) and (32), we write the required more accurate solution to the problem inside the target as

$$f_v\,(z,\mu,\phi) = K\left[z + 2\phi + \frac{1}{\varepsilon(x)}\left(\ln\frac{1+Y}{1-Y} - \ln\frac{1+\mu}{1-\mu}\right)\right]^{-\gamma_v}, \tag{34}$$

where $Y$ is to be found from (32), and the electric field is

$$\varepsilon(x) = \begin{cases} \varepsilon\,(\phi)\,, & \mu \geqslant 0\,, \\ \varepsilon\left(\dfrac{z\mu^2}{2}\right), & \mu < 0\,. \end{cases}$$

In the resultant distribution function (34), we segregate the angular distribution of energetic electrons [87]

$$f_v\,(z,\mu,\phi) = K\,(z+2\phi)^{-\gamma_v} H\,(z,\mu,\phi)\,, \tag{35}$$

where

$$H\,(z,\mu,\phi) = \left(1 + \frac{\ln\left[(1+Y)/(1-Y)\right] - \ln\left[(1+\mu)/(1-\mu)\right]}{\varepsilon\,(x)(z+2\phi)}\right)^{-\gamma_v}.$$

In Fig. 4, we show the angular distribution $H\,(z,\mu,\phi)$ of backward-flying ($\mu < 0$) electrons with energy $z$ in the plasma whose thickness corresponds to the potential $\phi$ in the target. We assume that the forward electrons ($\mu \geqslant 0$) are distributed isotropically. Then, as can be seen in Fig. 4, the distribution function of backward electrons becomes more isotropic as the depth increases; on the contrary, as the particle energy increases, the anisotropy increases, although it remains small. Strictly speaking, it is misleading to call such almost isotropic distributions of energetic electrons 'beams.' Instead, we refer to them as the 'energetic electron flow.'

We consider the question of the role of Coulomb collisions in the calculation of the distribution function. As noted in Section 3.1, condition (21) means that, at small depths, the regular losses of electrons due to collisions with particles of the background plasma are small compared to the energy losses in the reverse-current electric field. It is in this approximation that solution (27) was obtained. However, an important point is that the backward electrons, before arriving at the considered point $r$ in Fig. 3, were located at greater depths in the target, where they had lower energies and were exposed to a weaker electric field. Hence, collisions were essential for them, and condition (21) was inapplicable. Therefore, to correctly determine the distribution function $f_v$ at a large target thickness, we must accurately take collisions into account when finding the boundary function $f_{v\,bf}$, which amounts to using exact expressions (31) and (32) instead of (27).

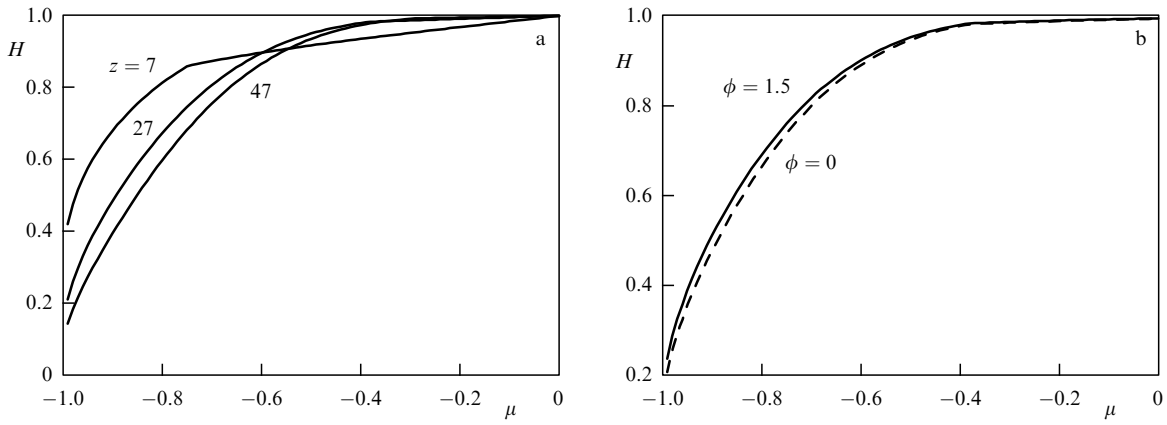


**Figure 4.** Angular distribution of backward-flying energetic electrons: (a) at different values of dimensionless energy $z$ at depth $\phi = 0$, (b) at different depths at dimensionless energy $z = 27$. Calculations were done with $\gamma_v = 4$.

However, in contrast to the classical problems that are one-dimensional in velocities (see Section 2.3), in the two-dimensional velocity problem discussed here, sufficiently fast electrons may be able to turn back while keeping the total speed greater than the thermal speed of electrons in the cold plasma. They manage to bypass the maximum energy loss in Coulomb collisions when the direction of motion is reversed. This is a fundamental feature of the two-dimensional velocity model of a thick target with a reverse current.

### 3.3 Electron acceleration in collapsing magnetic traps

**3.3.1 First-order Fermi acceleration and betatron heating.** Modern space observations of the Sun [33, 88, 89] have shown that the efficiency of acceleration of charged particles in the corona is extremely high. We have discussed the fact that, during a flare, the leading mechanism for converting magnetic energy into the kinetic energy of electrons is the electric field in the magnetic reconnection region. In many flares, however, taking this primary acceleration into account is insufficient for interpreting X-ray observations in the corona and the chromosphere.

In [67], a necessary additional mechanism for electron acceleration in a flare was proposed. Electrons were shown to acquire energy inside coronal magnetic traps as their size decreases in the longitudinal and transverse directions. This additional acceleration of electrons is due to two processes [90]: (a) first-order Fermi acceleration under longitudinal compression (reduction in length) of the magnetic trap and (b) betatron acceleration under transverse compression. Such a trap is shown schematically in Fig. 5 (cf. the trap in Fig. 2).

The physical nature of both processes, related to the applicability of the adiabatic approximation to solar flare conditions, is easy to understand. Following [67] (also see [29, 91]), let us estimate the period of particle motion between magnetic mirrors $M_1$ and $M_2$ (see Fig. 5) and its Larmor radius. As noted in Section 2.1 (see Fig. 1), the tops of the flare loops move toward the chromosphere with velocity $\mathbf{v}_1$. The characteristic speed is $v_1 \gtrsim 10^3$ km s$^{-1}$. Assuming the characteristic size of the trap to be $L_0 \sim 10^4$ km at the start of compression and $L = 0$ at its end, the trap lifetime is

$$t_{\rm trap} \approx \frac{L_0}{v_1} \lesssim 10 \text{ s}\,.$$

Assuming an average kinetic energy of the beam electrons of $\sim 30$ keV, which corresponds to the speed $v_e \approx 10^5$ km s$^{-1}$, we have the electron propagation time between the magnetic mirrors

$$\tau_{\rm trap} \approx \frac{2L_0}{v_e} \sim 0.1 \text{ s}\,.$$

Because $\tau_{\rm trap} \ll t_{\rm trap}$, the longitudinal size of the trap is virtually unchanged during the period of electron motion between the mirrors.

We now estimate the characteristic values of the Larmor radius of an electron. If the magnetic field at the top of the flare loop is $\sim 100$ G and increases to $\sim 800$ G toward the bases [64], then the Larmor radius of an electron is $r_L \sim 5$–$0.5$ cm. Evidently, $r_L \ll L_0$.

Therefore, the period of particle motion between the mirrors is much less than the lifetime of the trap, and the Larmor radius is much less than the length scales of magnetic field variations. Then, as the trap length decreases (Fig. 5a), the longitudinal adiabatic invariant is preserved,

$$p_\parallel L = p_{\parallel 0} L_0 = \text{const}\,, \tag{36}$$

and as the trap is compressed (Fig. 5b), the transverse invariant is preserved,

$$\frac{p_\perp^2}{B} = \frac{p_{\perp 0}^2}{B_0} = \text{const}\,. \tag{37}$$

Here, $p_\parallel$ and $p_\perp$ are the longitudinal and transverse momenta of the particle, $L_0$ and $B_0$ are the initial values of the trap length and the magnetic field inside it, and $L = L(t)$ and $B = B(t)$ are current values of the trap length and the magnetic field inside it.

Formulas (36) and (37) can be conveniently rewritten in dimensionless variables $b(t) = B/B_0$ and $l(t) = L/L_0$ as

$$p_\parallel = \frac{p_{\parallel 0}}{l}\,, \tag{38}$$

$$p_\perp = p_{\perp 0}\sqrt{b}\,. \tag{39}$$

It is clear on general grounds that $l \leqslant 1$ and $b \geqslant 1$. Expression (38) corresponds to first-order Fermi acceleration: as the trap length $l$ decreases with time, the longitudinal momentum of the particle increases and the transverse momentum remains constant. On the contrary, betatron acceleration (39) results in an increase in the transverse momentum and leaves the longitudinal momentum unchanged. Both mechanisms operate simultaneously in solar flares (see Fig. 2).

Formulas (38) and (39) characterize the increase in the momentum and hence in the kinetic energy of an electron trapped in a collapsing magnetic trap. We now determine the change in its pitch angle under the combined action of the two acceleration mechanisms. For this, we use dimensionless

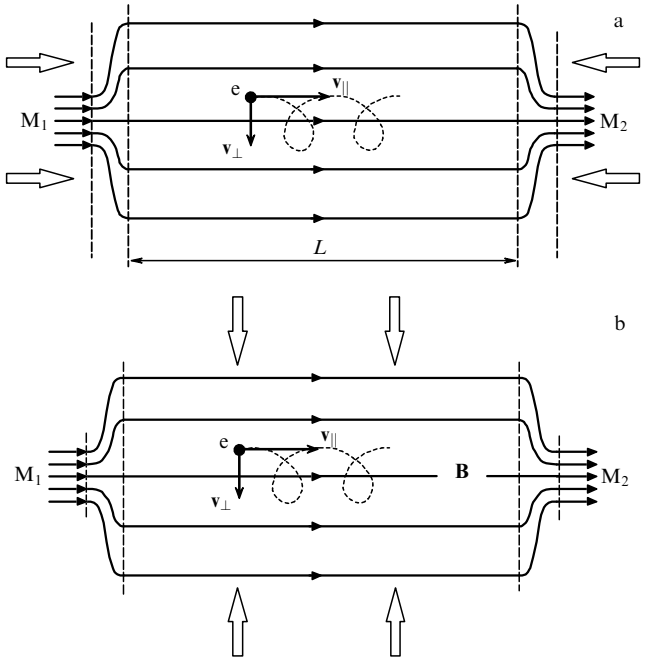


**Figure 5.** Schematic representation of a magnetic trap collapsing in (a) longitudinal and (b) transverse directions. $L$ is the trap length, $\mathbf{B}$ is the magnetic field, $\mathbf{v}_\perp$ and $\mathbf{v}_\parallel$ are the transverse and longitudinal components of the velocity vector of electron e whose trajectory is conventionally shown with a dotted line, and $M_1$ and $M_2$ are magnetic mirrors (plugs).

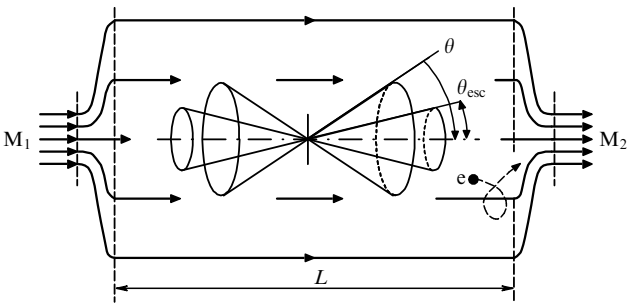


**Figure 6.** Schematic representation of a magnetic trap retaining energetic electrons. Electrons with a pitch angle $\theta \leqslant \theta_{\rm esc}$ pass freely through magnetic mirrors $M_1$ and $M_2$ and leave the trap. Electrons with a pitch angle $\theta > \theta_{\rm esc}$ remain trapped.

variables to write

$$\tan\theta = \frac{p_\perp}{p_\parallel} = l\sqrt{b}\left(\frac{p_{\perp 0}}{p_{\parallel 0}}\right) = l\sqrt{b}\tan\theta_0\,, \tag{40}$$

where $\theta_0$ and $\theta$ are the respective initial and current pitch angles of the electron. It follows from (40) that, for $l\sqrt{b}=1$, the trap does not alter the angular distribution of energetic electrons. If $l\sqrt{b}<1$, then the pitch angle becomes smaller as the trap is compressed, and the first-order Fermi mechanism is dominant. On the contrary, for $l\sqrt{b}>1$, the pitch angle increases and the betatron acceleration becomes dominant.

The electron is trapped and accelerates until it reaches the loss cone (Fig. 6). The tangent of the pitch angle at that instant is given by [91]

$$\tan\theta_{\rm esc} = \frac{1}{\sqrt{b_{\rm m}/b-1}}\,, \tag{41}$$

and the kinetic energy, written in dimensionless form, is

$$z = z_0\, b_{\rm m}\,(1-\mu^2)\,. \tag{42}$$

Here, $z_0$ is the initial energy of the electron; the mirror ratio is $b_{\rm m} = B_{\rm m}/B_0$, where $B_{\rm m}$ is the magnitude of the magnetic field in the mirrors. Electrons with a pitch angle $\theta \leqslant \theta_{\rm esc}$ pass through them freely and precipitate into the chromosphere, where they lose energy in Coulomb collisions and generate hard X-ray bremsstrahlung of the solar flare.

To conclude the general discussion of acceleration processes in collapsing coronal magnetic traps, we recall two nontrivial features inherent in these processes [90, 91].

First, the transverse compression of a collapsing trap is attended by betatron heating, but has no effect on the energy acquired by the electron during acceleration due to a decrease in the trap length. The electron energy at the instant of escape from the trap remains the same as it would be in a collapsing trap without compression [90]. This is due to an increase in the loss cone, resulting in an earlier escape of the electron from the trap, which is nevertheless exactly compensated by a faster increase in maximum energy (42) due to betatron heating.

This does not imply the absence of observational manifestations of betatron acceleration. On the contrary, in a trap with betatron heating, the concentration of trapped electrons and their integrated kinetic energy reach values that are several times higher [91] than their maximum possible values in a trap where Fermi acceleration dominates. We can therefore expect significantly higher intensities of hard X-ray radiation generated by trapped electrons during their collisions with thermal plasma particles. In other words, in flares exhibiting a bright coronal source of hard X-ray radiation, it is reasonable to assume the presence and high efficiency of betatron heating of energetic electrons.

Second, it follows from formula (42) that the maximum energy $z_{\max} = z_0\, b_{\rm m}$ acquired by electrons in a collapsing trap depends only on the mirror ratio $b_{\rm m}$. As noted in [91], $b_{\rm m}$ can reach values $\gtrsim 100$, providing electron acceleration to energies of $\sim 1$ MeV.

**3.3.2 Distribution function of electrons in a collapsing trap.** It was shown in [91] that, as the size of a trap decreases (as described by the dimensionless variables $l(t)$ and $b(t)$), the number of energetic electrons trapped in it is

$$N(t) = N_0\,\frac{l\sqrt{b_{\rm m}-b}}{\sqrt{1+(b_{\rm m}-b)\,l^2}}\,, \tag{43}$$

and their distribution function is given by

$$f_{\rm v}\,(t,z,\mu) = \frac{l}{b}\,f_{\rm v0}\,(z\,\mathcal{A}_\mu)\,, \tag{44}$$

where

$$\mathcal{A}_\mu = \frac{1+(bl^2-1)\mu^2}{b}\,,$$

$N_0$ is the initial number of particles in the trap, and $f_{\rm v0}$ is the boundary distribution function (see (10) and (33)).

As is known, magnetic reconnection in the current layer of a flare does not occur monotonically but in jumps, in the form of successive pulses [29], during which separate tubes of reconnected magnetic field lines — collapsing traps — are formed. It follows from (43) that, depending on the value of the mirror ratio $b_{\rm m}$, each such trap, during its existence, can retain up to 99% of electrons coming from the current layer (see Fig. 3 in [91]). Thus, the trap can significantly reduce the flux of energetic electrons precipitating from it into the chromosphere. As a result, the intensity of bremsstrahlung of energetic electrons in the chromosphere is reduced to a minimum. Therefore, time instants can occur when there is almost no hard X-ray emission from the chromospheric base of an individual collapsing trap in the presence of a bright source at its coronal top. However, in many flares, due to the superposition of traps in different phases of their evolution, the observed pattern is much more complex and diverse.

Formula (44) was used in [92] to find the ratio of the distribution functions of electrons at the current instant and at the instant of injection:

$$f_{\rm v}\,(z) = \frac{N_0}{N}\,\frac{l}{b}\int_0^{\sqrt{1-b/b_{\rm m}}} f_{\rm v0}\,(z\mathcal{A}_\mu)\,{\rm d}\mu\,. \tag{45}$$

Formula (45) can be used with any initial velocity distribution $f_{\rm v0}$ of energetic electrons. Substituting boundary condition (10), corresponding to a power-law injection spectrum, into (45), we find the normalization constant (see (11)) of the distribution function of accelerated electrons inside a collapsing magnetic trap:

$$K' = K\sqrt{\frac{1+(b_{\rm m}-b)l^2}{b\sqrt{b_{\rm m}-b}}}\int_0^{\sqrt{1-b/b_{\rm m}}}\left[\frac{1+\mu^2(bl^2-1)}{b}\right]^{-\gamma_{\rm v}}{\rm d}\mu\,. \tag{46}$$

Thus, the exponent of the slope of the power spectrum of electron injection during their additional acceleration inside a collapsing magnetic trap remains a power-law one with the same exponent $\gamma_v$, while the coefficient $K$ increases in accordance with formula (46). This feature of electron acceleration is an important observational manifestation that allows estimating the presence and efficiency of collapsing magnetic traps in the coronal part of flare loops.

### 3.4 Specific features of the combined model

In Sections 3.2 and 3.3, we presented a self-consistent kinetic model of electron propagation in solar flares where the effect of the reverse current electric field as well as acceleration in collapsing magnetic traps formed at the tops of flare loops were taken into account. We now discuss the features of such a combined model.

Already in pioneering studies [63, 84, 93], it was shown at the level of simple estimates that the reverse current that compensates the electric current associated with the flow of accelerated electrons must be taken into account. Indeed, in its absence, beams of accelerated electrons would have generated unacceptably large electric currents ($\gtrsim 10^{17}$ A) and hence huge magnetic fields, which are not observed in solar flares [34, 64, 94].

To self-consistently calculate the reverse-current electric field and its effect on the process of propagation of energetic electrons in the solar atmosphere, with their Coulomb collisions with thermal plasma particles taken into account, we cannot restrict ourself to simple models that deal with only the mean rates of energy variation and scattering for fast electrons but ignore the dispersion of mean values [95]. It is necessary (see Sections 2.2 and 3.2) to accurately solve the corresponding two-dimensional velocity problem [62, 65, 66, 87]. As we show below, this is especially important when calculating sensitive characteristics such as the spectrum and polarization of the bremsstrahlung of energetic electrons, primarily for the purpose of characterizing them based on satellite observations of the Sun in the hard X-ray range.

The reverse current significantly affects the nature of the propagation of accelerated electrons in the solar atmosphere. Due to the predominance of energy losses in the reverse-current electric field over the energy losses in Coulomb collisions, the values of the electron distribution function obtained in the reverse-current model must be much greater than those obtained in the classical thick-target approximation. The flux density of energetic electrons in the reverse-current model is much higher than that in the classical thick-target model without the reverse current. The distribution function of energetic electrons becomes more isotropic as they penetrate into the target; in contrast, its anisotropy increases with an increase in their energy (see Fig. 4).

Progress in the quality, resolution, and sensitivity of modern electromagnetic radiation receivers aboard spacecraft studying the Sun has resulted in a steadily increasing number of flares [96] in which bright coronal sources of hard X-ray radiation are detected (see [24] for the first observations). Such flares can be naturally interpreted in terms of kinetic models with collapsing magnetic traps in the corona. When compressing, the traps not only effectively retain electrons but also increase their total kinetic energy; taken together, these factors significantly increase the intensity of hard X-rays in the coronal source.

Depending on the flare rating, the duration of its impulsive phase varies widely and can be $\gtrsim 100$ s on average. During this time, several collapsing traps are created and destroyed in the corona (see Section 3.3.1). During observation of the impulsive phase of a flare, the intensities of the coronal and chromospheric hard X-ray sources undergo multiple changes. But in the absence of instruments ensuring sufficient spatial and temporal resolution, it is impossible to trace the development of each collapsing trap separately. Therefore, when interpreting observations, we understand a 'trap model' as the average over an ensemble of collapsing traps present in a flare in the time interval specified by averaging.

To estimate the efficiency of electron acceleration in such an 'averaged collapsing trap' [92], we must estimate its mirror ratio $b_m$, which is typically not known from observations. We tune this free model parameter such that the calculated intensity of hard X-ray radiation in the corona corresponds to the maximum to the observed one. In addition, estimates of the effective compression parameters $b_{eff}$ and $l_{eff}$ of the averaged trap allow estimating the relative roles of Fermi acceleration and betatron heating. The simplifications listed above give rise to a certain freedom in interpreting observations, which has its own merits and opens up a realistic possibility of understanding the peculiarities of the physics associated with accelerating energetic electrons in collapsing traps.

In this section, we present a combined self-consistent kinetic model for the propagation of energetic electrons, with the reverse current taken into account. It is given by analytic solution (34) of the kinetic problem in (3)–(5), (9) with boundary condition (10). It was shown in [71, 72] that the found solution well describes the distribution function both at small thicknesses in the target ($s \sim 0$, thin-target approximation) and at large thicknesses ($s \to \infty$, thick-target approximation with reverse current). In the first case, the boundary distribution function is virtually unchanged by the action of the reverse-current electric field and Coulomb collisions, and is given by relations (10) and (33). In the second case, as accelerated electrons propagate in the corona and the chromosphere, the distribution function changes significantly (see (34)) due to the action of the reverse-current electric field on the accelerated electrons and Coulomb collisions with plasma electrons and ions.

Importantly, the combined model takes the effect of additional acceleration of electrons in collapsing traps into account. The thin-target model is complemented by the model of a collapsing magnetic trap, in accordance with (46). The solutions presented in this section can be used to model specific solar flares and interpret X-ray data. For this, the energy flux density $F$ and the slope exponent $\gamma_v$ of the injection spectrum must be chosen such that the model characteristics of the hard X-ray spectrum of the chromospheric source fit the observational data. Based on these results, the spectrum parameters of the coronal source can then be calculated. We recall that the model parameters are the superhot and cold plasma temperatures $T_1$ and $T_2$, the cold plasma density $n_2$, and the mirror ratio $b_m$.

## 4. Hard X-ray emission from solar flares

Accelerated electrons propagating along flare loops generate bursts of hard X-ray bremsstrahlung, whose characteristics are determined by the evolution of the flux of these particles. In Section 3, we presented a combined kinetic model that allows accurately describing these processes and calculating

the characteristics of the generated radiation. In what follows, as an example, we calculate the spectra of hard X-ray emission for two especially selected solar flares, those of December 6, 2006 and July 19, 2012. Also, in the conclusion of this section, we separately discuss the expected polarization values for solar flares in general and the prospects for polarization measurements in future experiments.

The observational data used in this section are based on hard X-ray observations with the Ramaty High-Energy Solar Spectroscopic Imager (RHESSI) [52] and on optical-range observations using the Solar Dynamics Observatory (SDO) [53]. In addition, whenever data were available, observations from the Hinode [97], Geostationary Operational Environmental Satellite (GOES) [98], and Transition Region and Coronal Explorer (TRACE) [99] satellites were used. The high spatial, temporal, and spectral resolutions of space observatories allow accurately determining the position and size of radiation sources during the impulsive phase of a flare, as well as the characteristics of their spectra. The flares of December 6, 2006 and July 19, 2012 were chosen for modeling due to the abundance and accuracy of observations. Furthermore, an important point is that the first of them is located on the solar disk and the second on the limb.

### 4.1 Method for calculating bremsstrahlung characteristics

Based on distribution function (34), we describe the strategy for calculating the characteristics of hard X-ray bremsstrahlung. Let $\mathcal{E}_v = hv/k_B T_1$ be the dimensionless photon energy and $\vartheta$ be the angle between the wave vector $\mathbf{k}$ and the electron velocity $\mathbf{v}$. In [100], the differential cross sections for the bremsstrahlung of photons polarized parallel and perpendicular to the $(\mathbf{v}, \mathbf{k})$ plane are given in the form

$$\frac{\partial^2 \sigma_\parallel}{\partial\Omega\, \partial(hv)} = C\,(A + B\sin^2\vartheta)\,\sigma_0\,,$$

$$\frac{\partial^2 \sigma_\perp}{\partial\Omega\, \partial(hv)} = CA\,\sigma_0\,,$$

where

$$A = \frac{z - \mathcal{E}_v/2}{\sqrt{z(z-\mathcal{E}_v)}} \ln\frac{\sqrt{z} + \sqrt{z-\mathcal{E}_v}}{\sqrt{z} - \sqrt{z-\mathcal{E}_v}} - 1\,,$$

$$B = \frac{(3/2)\,\mathcal{E}_v - z}{\sqrt{z(z-\mathcal{E}_v)}} \ln\frac{\sqrt{z} + \sqrt{z-\mathcal{E}_v}}{\sqrt{z} - \sqrt{z-\mathcal{E}_v}} + 3\,,$$

$$C = \frac{1}{z\mathcal{E}_v} \frac{1 - \exp\left(-2\pi\alpha c\sqrt{m_e/2z\,k_B T_1}\right)}{1 - \exp\left(-2\pi\alpha c\sqrt{m_e/2\,(z-\mathcal{E}_v)\,k_B T_1}\right)}\,,$$

$$\sigma_0 = \frac{\alpha}{2\pi}\frac{m_e c^2}{k_B T_1}\frac{r_0^2}{k_B T_1}\,,$$

$\alpha = e^2/\hbar c$ is the fine structure constant, $r_0 = e^2/m_e c^2$ is the classical electron radius, and $\partial\Omega$ is the solid angle element.

Let $I_{HXR\,\parallel}$ and $I_{HXR\,\perp}$ be hard X-ray fluxes of the source under study with polarizations parallel and perpendicular to the plane defined by the line of sight (direction from the radiation source to the observer) and the magnetic field in the source, i.e., the direction of propagation of the electron flow (Fig. 7). Then, according to the formulas derived in [101], the

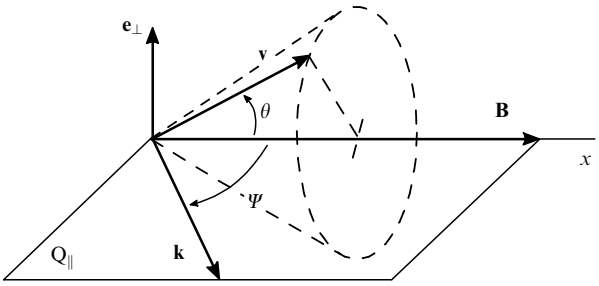


**Figure 7.** Conventional picture of emission. **k** is the wave vector of an X-ray photon, $\Psi$ is the angle between the line of sight and the direction of propagation of the runaway electron flow ($x$-axis in Figs 1 and 3), $\theta$ is the pitch angle of the electron, $Q_\parallel$ is the plane of parallel polarization of radiation, and $\mathbf{e}_\perp$ is the normal to the $Q_\parallel$ plane.

total flux of hard X-ray radiation is

$$I = I_\perp + I_\parallel = \kappa\left[8\int_{hv}^{\infty} AC\left(\int_0^\infty L_0\,\mathrm{d}\xi\right) z\,\mathrm{d}z + \frac{8}{3}\int_{hv}^{\infty} BC\left(\int_0^\infty L_0\,\mathrm{d}\xi\right) z\,\mathrm{d}z + \frac{12\,\sin^2\psi - 8}{15}\int_{hv}^{\infty} BC\left(\int_0^\infty L_2\,\mathrm{d}\xi\right) z\,\mathrm{d}z\right], \quad (47)$$

and the difference among polarized fluxes is

$$I_\perp - I_\parallel = -\frac{4}{5}\,\kappa\sin^2\psi\int_{hv}^{\infty} BC\left(\int_0^\infty L_2\,\mathrm{d}\xi\right) z\,\mathrm{d}z\,. \quad (48)$$

Here, $\psi$ is the angle between the line of sight and the direction of propagation of the flow of runaway electrons, and $L_0 = L_0(z,\phi)$ and $L_2 = L_2(z,\phi)$ are the coefficients of the distribution function expansion in a series in Legendre polynomials. The plasma thickness $\xi$ along the magnetic field from the turbulent front boundary to a certain depth $r$ (see Fig. 3) is given by

$$\xi(r)\ [\mathrm{cm}^{-2}] = \int_0^r n_2(x)\,\mathrm{d}x\,, \quad (49)$$

where the integral is taken along the magnetic field. The use of $\xi$ in the thick-target model considered here is very convenient, because it allows avoiding assumptions about the distribution of the plasma concentration in the target [12] and the length of the X-ray source. In (47) and (48), the upper integration limit for the source thickness $\xi$ is equal to infinity. The quantity

$$\kappa = \frac{\alpha}{\pi}\left(\frac{r_0}{R}\right)^2 m_e c^2\,\frac{K S_{HXR}}{m_e^2}$$

has the dimension photon $\mathrm{keV}^{-1}\ \mathrm{s}^{-1}$ (the expression in square brackets in (47) has the dimension $\mathrm{cm}^{-2}$), $R$ is the distance from the Sun, and $S_{HXR}$ is the characteristic area of the radiation source.

From the standpoint of testing the initial assumptions of the model, a primary characteristic of the hard X-ray spectrum is its slope. It can be measured directly, and it also characterizes the process of electron acceleration, because it is determined by the electron distribution function. If solution (14) is substituted into (47), then it is not difficult to obtain classical hard X-ray bremsstrahlung spectra for the respective

thick- and thin-target models as $s \to \infty$ and $s \to 0$. In the framework of classical flare models, the corresponding formulas were obtained in [12, 61], where, in particular, the following well-known relations for the spectral slope exponents are given:

$$\varphi_{\rm Cor} = \gamma_{\rm SS} + 1 \quad \text{for a thin target}\,, \tag{50}$$

$$\varphi_{\rm Ch} = \gamma_{\rm SS} - 1 \quad \text{for a thick target}\,. \tag{51}$$

To avoid confusion, we also fix the relation between the slope exponents of the injection spectra:

$$\gamma_{\rm SS} = \gamma_{\mathcal{E}} - \frac{1}{2} = \gamma_{\mathbf{v}} - 1\,, \tag{52}$$

where $\gamma_{\rm SS}$ is the slope exponent of the energy spectrum of the accelerated electron flux and $\gamma_{\mathcal{E}}$ is the slope exponent of the energy spectrum of the density of accelerated electrons (see (10)). Recall that the exponent $\gamma_{\mathbf{v}}$ characterizes the distribution of particles, not by energy but by velocity vector $\mathbf{v}$ in the two-dimensional velocity space.

### 4.2 Solar flare of December 6, 2006

**4.2.1 Flare observations.** A white (most of the energy being emitted in the optical continuum; see, e.g., [89, 102, 103]), class X6.5 flare was observed on December 6, 2006 simultaneously in different ranges of the electromagnetic spectrum at the Hinode and GOES space observatories, TRACE, and RHESSI. At the instant of the maximum hard X-ray emission, there were observations of a source with a very high spatial resolution: $\approx 0.2''$ for the SOT optical telescope on the Hinode satellite, and $\approx 1''$ for the X-ray telescope on the RHESSI satellite. The results of these observations and data processing methods are described in [104]. The observational data used were obtained by adding the results of individual measurements over a time interval of 8 s, centered on the main maximum of the hard X-ray burst.

The flare image in the hard X-ray range consists of two flare ribbons, which are shown in Fig. 8a. The brightest radiation source is located in the southern ribbon, whose angular size was determined with high accuracy. According to [104], its area is $S_{\rm HXR} \approx 1.5 \times 10^{16}$ cm$^2$, with the angular size $\approx 1.1''$. The lower bound of the accelerated electron injection spectrum $\mathcal{E}_{\rm min} = 18$ keV is estimated with a rather large error of $\pm 3$ keV, which is due to the superposition of the thermal and nonthermal emission spectra. As noted, the injection spectra have large slope exponents, and hence simulation results are weakly sensitive to errors in the choice of the upper energy bound, which we set equal to $\mathcal{E}_{\rm max} = 120$ keV.

The temperature of the cold plasma in the target ahead of the turbulent front (see Figs 1 and 3) is quite high, $T_2 = 37.4 \pm 0.4$ MK. The temperature of the source of accelerated electrons, i.e., the superhot plasma behind the turbulent front, is not known from observations and is assumed to be $T_1 = 100$ MK, which is an order-of-magnitude estimate based on the theory of reconnecting superhot turbulent current layers [29, Section 8.5]. The concentration of cold plasma particles in the target is poorly known; we assume that it is equal to the characteristic value in the upper chromosphere: $n_2 \approx 2 \times 10^{10}$ cm$^{-3}$.

The brightest source of hard X-ray radiation, located on the southern flare ribbon (Fig. 8b), is of particular interest to us because, being of a relatively small size, it generates hard X-ray radiation with a high energy flux ($12 \pm 2$ photon cm$^{-2}$ keV$^{-1}$ at a photon energy of 50 keV) and the spectrum slope exponent $\varphi_{\rm Ch} = 2.6 \pm 0.2$. We now proceed to our results of modeling the spectral properties of the source.

**4.2.2 Hard X-ray radiation spectrum.** The presented observational data, combined with formulas for distribution function (34), boundary condition (10), reverse current electric field (29), and emission spectrum (47), allow reconstructing the injection spectrum of electrons accelerated in the flare on December 6, 2006, describing the change in the spectrum with the depth of penetration into the target, and calculating the plasma heating power in the target.

Figure 9 shows the results of observations and calculation of the hard X-ray spectrum for a bright source on the southern flare ribbon. The theoretical straight line approx-

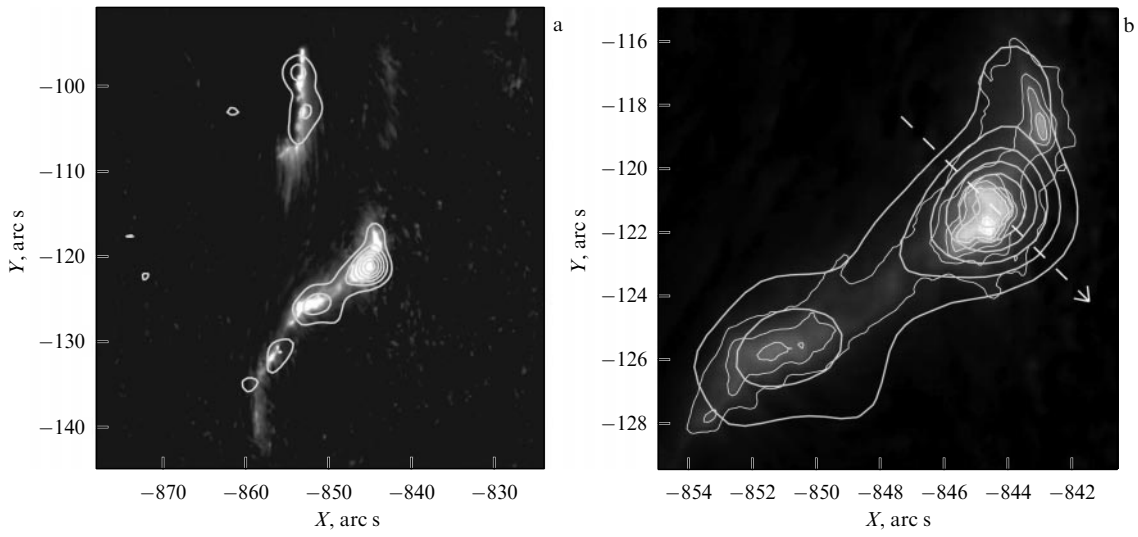


**Figure 8.** Images of the flare on December 6, 2006 in the G band (4305 Å) obtained by the Hinode satellite using the SOT optical telescope. (a) Entire flare area. (b) Southern flare ribbon with the brightest radiation source. Bold contours show levels of hard X-ray radiation according to the RHESSI satellite data (15%, 30%, 45%, 60%, 75%, and 90% of the maximum intensity). Angular size of the main source is determined along the dashed arrow. Images taken from [104].

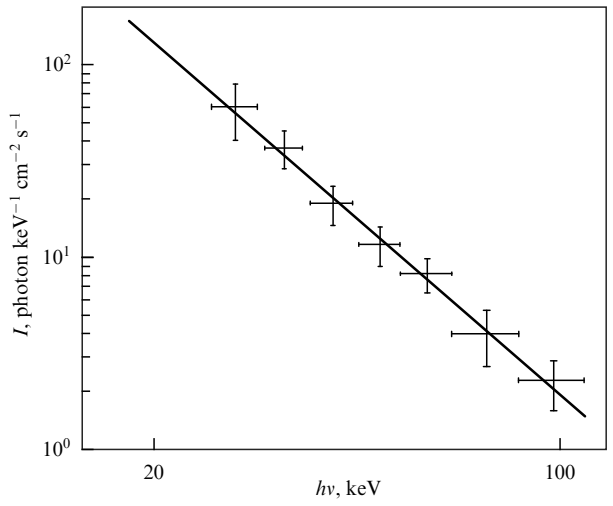


**Figure 9.** Hard X-ray spectrum of the December 6, 2006 solar flare. Simulation results are shown with a straight line, observational results are represented by points with error bars.

imates the observational data with high accuracy, which indicates the correct tuning of the model parameters: the energy flux density $F$ carried by the accelerated electrons and the slope exponent $\gamma_v$ of the injection spectrum. In Table 1, for comparison, these results are presented together with those of calculations done in the framework of the classical thick-target model.

We estimate the ratio of the gas pressures $p_1$ and $p_2$ at the boundary of the turbulent front (see Fig. 3) between the superhot plasma of the accelerated electron source and the colder target plasma. According to [105], the concentration of superhot plasma particles is somewhat higher than the coronal one, namely, $n_1 \sim 10^9$ cm$^{-3}$. In accordance with the data in Section 4.2.1, we then find

$$p_1 \sim p_2 \,. \tag{53}$$

The equality of pressures in the hot and cold plasmas implies that the cold plasma is heated relatively slowly at the short time scales considered in this paper. Given the relatively small thickness of the turbulent layer, it is unsurprising that the pressure has enough time to equalize due to the hydrodynamic expansion of the heated plasma within the layer. For slow heating, in turn, we should expect small values of the reverse-current electric field (see (29)). For the December 6, 2006 flare, the dimensionless electric field is $\varepsilon \approx 1.5$. A field of such a relatively low strength, however, exerts a noticeable effect on the propagation of beam electrons.

**4.2.3 Spectra of accelerated electrons and plasma heating power.** Let us discuss in somewhat greater detail the features of the propagation of accelerated electrons injected into the cold target plasma during the flare on December 6, 2006. The magnitude of the electric field of the reverse current and the parameters of the injection spectrum were calculated in Section 4.2.2 in the approximation of a thick-target model with a reverse current (see formulas (29) and (10)). In addition, the parameters of the injection spectrum were determined for comparison in the approximation of the classical thick-target model [61] without reverse current (see Table 1). Based on these data, we now calculate the change in the energy spectrum of electrons depending on the plasma thickness in the target and the plasma heating power in it for both models.

We write the definition of the concentration (the number of particles in a unit volume) in a flow of energetic electrons ([28, Section 4.3.2]),

$$n_b(\xi) = \int_0^\infty \pi \left(\frac{2k_B T_1}{m_e}\right)^{3/2} \int_{-1}^{1} f_v(z,\xi,\mu)\sqrt{z}\,d\mu\,dz\,. \tag{54}$$

The integrand in (54) is the differential energy spectrum of the injected electrons and its variation depending on the plasma thickness $\xi$:

$$N(z,\xi) = \frac{\pi}{m_e}\left(\frac{2k_B T_1}{m_e}\right)^{1/2} \int_{-1}^{1} f_v(z,\xi,\mu)\sqrt{z}\,d\mu\,. \tag{55}$$

Figure 10 shows the energy spectra of electrons accelerated in the flare on December 6, 2006. The calculation results were obtained using formula (55) with distribution function (34) and solution (14) of the classical thick-target model without reverse current.

In the classical model (see Fig. 10), the injection spectrum has the slope exponent $\gamma_\mathcal{E} \approx 4.1$ and the concentration of energetic electrons in the flow $n_b \approx 1.4 \times 10^{10}$ cm$^{-3}$. In the thick-target model with reverse current, the injection spectrum is harder, $\gamma_\mathcal{E} \approx 3.2$, and the concentration is an order of magnitude higher: $n_b \approx 1.9 \times 10^{11}$ cm$^{-3}$. Such significant differences in the spectra are due to the reverse-current electric field, whose action allows some of the electrons to effectively lose their kinetic energy along the magnetic field, and some of them turn back with virtually no energy loss.

Figure 10 shows that, even for a small plasma thickness in the target, $\xi = 3 \times 10^{19}$ cm$^{-2}$, the electron spectra of the two models (dashed line) differ significantly. The effect is especially pronounced in the model that takes the reverse-current electric field into account: we see a significant shift of the spectrum toward low energies, where it becomes harder. Therefore, in the thick-target model with a reverse current, huge fluxes of accelerated electrons with a harder injection spectrum are needed to ensure the observed intensity of nonthermal hard X-ray radiation. Such fluxes contain a sufficiently large number of high-energy electrons that are capable of penetrating into the chromosphere to the depth of the optical region of the flare under the effect of the reverse-current electric field.

We calculate the heating of the cold target plasma by accelerated electrons using a formula for the heating power in [61],

$$\mathcal{P}(\xi)\ [\text{keV s}^{-1}] = \frac{4\pi a_0}{m_e^2}\,(k_B T_1)\int_0^\infty \int_{-1}^{1} f_v(z,\xi,\mu)\,dz\,d\mu\,, \tag{56}$$

**Table 1.** Characteristics of electrons accelerated in the flare on December 6, 2006 in thick-target models with and without reverse current.

| Model | $\gamma_v$ | $\gamma_\mathcal{E}$ | $\gamma_{SS}$ | $n_b$, cm$^{-3}$ | $F$, erg cm$^{-2}$ s$^{-1}$ | $\varphi_{Ch}$ |
|---|---|---|---|---|---|---|
| Without reverse current | 4.6 | 4.1 | 3.6 | $1.4 \times 10^{10}$ | $2.2 \times 10^{12}$ | 2.6 |
| With reverse current | 3.7 | 3.2 | 2.7 | $1.9 \times 10^{11}$ | $3.5 \times 10^{13}$ | 2.6 |

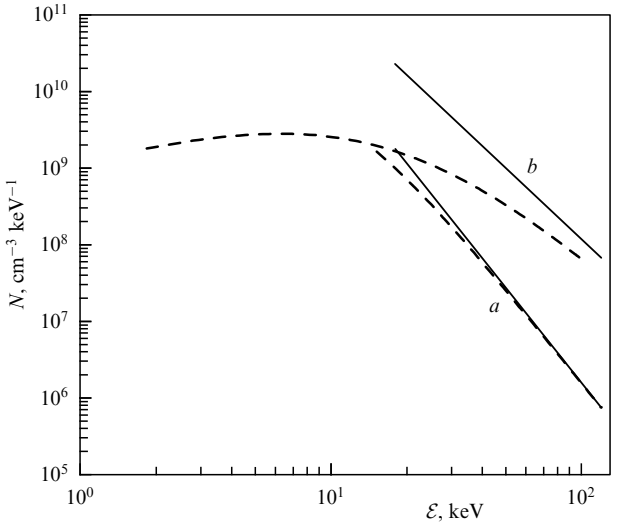


**Figure 10.** Energy spectra of accelerated electrons: (*a*) classical thick-target model; (*b*) thick-target model with reverse current. Solid line shows the injection spectrum, dashed line shows the spectrum of electrons at plasma thickness $\xi = 3 \times 10^{19}$ cm$^{-2}$.

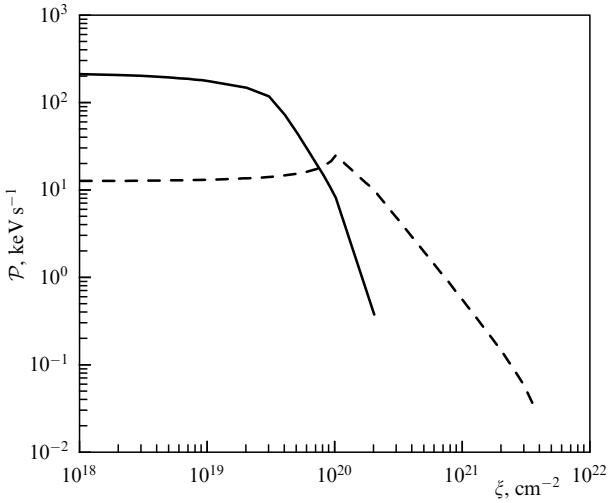


**Figure 11.** Power of plasma heating by accelerated electrons in the flare of December 6, 2006, calculated in the thick-target model: dashed line — without reverse current, solid line — with reverse current.

with the coefficient

$$a_0\ [\mathrm{keV^2 cm^2}] = 2\pi e^4 \ln \Lambda \approx 1.3 \times 10^{-19} \times \left[ \ln\left(\frac{\mathcal{E}}{m_\mathrm{e} c^2}\right) - \frac{1}{2} \ln n_2 + 38.7 \right].$$

In the thick-target model with a reverse current, the pattern of plasma heating is very different from the one resulting from calculations in the classical model without reverse current (Fig. 11). The heating power in the reverse-current model is very high and remains almost constant up to a relatively small plasma thickness $\xi \sim 10^{19}$ cm$^{-2}$, after which a sharp decrease in the energy release is observed. In the classical model, energetic electrons penetrate through an order-of-magnitude larger thickness, where they produce maximum heating. Note that, due to the lack of data on the distribution of the plasma density inside the target, we did not estimate the heating of the target by the reverse current due to Coulomb collisions of the particles of the background plasma with the particles that create the reverse current (however, see [85]). Nevertheless, near the target boundary ($\xi = 0$), where the density of the surrounding plasma is approximately known ($n_2 \approx 2 \times 10^{10}$ cm$^{-3}$), the power heating by reverse current can reach large values ($\sim 100$ keV s$^{-1}$).

The high heating power at small thickness in the thick-target model with a reverse current is associated not only with an initially order-of-magnitude higher energy flux carried by forward electrons but also largely with energetic electrons that turned under the action of the electric field and move back to the source. Of course, there are many more such electrons than in the case of the classical model without reverse current (see Section 3, Fig. 4). Many of them ($n_\mathrm{bf} \approx 6 \times 10^{10}$ cm$^{-3}$) return to the target boundary and may then overcome the turbulent front and return to the source.

Thus, taking the reverse current into account when simulating powerful events such as the December 6, 2006 flare allows obtaining realistic estimates for the energy fluxes at the target boundary. These energy fluxes provide a high level of heating of the hard X-ray source and may also be sufficient to explain the optical (white) flare. Indeed, at depths characteristic of the chromosphere, i.e., for a plasma thickness of $\sim 10^{20}$ cm$^{-2}$, where the electric field of the reverse current tends to zero (see (29)), the number of energetic electrons with energies up to 90 keV is still large, $\sim 10^9$ cm$^{-3}$. At greater depths in the chromosphere, the change in the spectrum is determined solely by Coulomb collisions.

In [106], the results of a statistical analysis of the dependence of superhot plasma parameters on the power of solar flares are presented. Based on the RHESSI space observatory data, using 37 flares as an example, it is shown that, as the flare intensity increases from class M1.0 to X10.0, the maximum plasma electron temperature increases from $\sim 20$ MK to $\gtrsim 50$ MK. Of course, this concerns some average plasma temperature between the reconnecting current layer and the turbulent front, because the emission of the superhot current layer is very low [107].

In view of the large fluxes of energetic electrons in powerful flares of class X, we can assume a reverse-current electric field $\varepsilon > 1$. In powerful flares, therefore, the plasma appears to be heated in accordance with the thick-target model with a reverse current (see Fig. 11). The energetic electrons returning to the source and the reverse-current electrons (i.e., thermal plasma electrons accelerated by the reverse-current electric field) effectively heat the coronal plasma to anomalously high temperatures. The energetic electrons that escaped into the lower corona and the chromosphere are responsible for heating the plasma to somewhat lower temperatures.

Similar results are presented in [78] for a less powerful (M3.5) solar flare on February 24, 2006. It is shown that the coronal plasma is heated to temperatures of $\sim 20$ MK not only near the turbulent front but also in the chromospheric bases of a system of collapsing magnetic traps. However, plasma heating by energetic electrons is apparently less efficient in class-M flares than in class-X flares and depends less significantly on the rate-M flare power.

A high concentration of forward electrons in the reverse-current model (see Table 1) and a significant concentration of electrons returning to the source can play a decisive role in interpreting X-ray observations in the corona, because the emission from a coronal hard X-ray source is much lower

than in the case of the classical model without reverse current. We therefore proceed to discussing a flare located on the solar limb with a bright coronal source of hard X-rays.

### 4.3 Solar flare of July 19, 2012

**4.3.1 Flare observations.** The M7.7 flare on July 19, 2012 was observed with the instrumentation at the RHESSI, GOES, and SDO space observatories starting from its onset at 05:15 UT. The high accuracy of modern multiwave radiation detectors and the location of the flare at the edge of the solar disk allowed observing bright compact radiation sources and extended flare loops simultaneously in the corona and the chromosphere with high temporal, spatial, and spectral resolution [108–111].

Let us consider the observed flare pattern (Fig. 12). In the hard X-ray range, one coronal and two chromospheric sources can be seen. The southern chromospheric source is very weak, because it is partially located behind the limb. We study the north chromospheric radiation source using the thick-target model approximation with reverse current (see Section 3.2). As in Section 4.2, we tune the energy flux density of accelerated electrons such that the spectrum of the chromospheric radiation source fits the observational data. Observations from the RHESSI satellite are presented in [110] as the sum of individual measurements with a duration of $\sim 8$ s over a time interval of $\sim 150$ s, shown in Fig. 12a with a dark vertical band centered at the first maximum of the hard X-ray burst at 05:21:45 UT.

The chosen time interval corresponds to that part of the flare impulsive phase when the electron acceleration process is most efficient and the intensity of hard X-ray bremsstrahlung is maximum. Compared to this time interval, the total duration of the impulsive phase is large, $\sim 10^3$ s (see Fig. 12 and also [109]). Generally speaking, this allows assuming a relatively slow process of magnetic reconnection in this flare and hence the absence of an SW-type shock wave shown in Fig. 2 (see also [29, 67]).

The coronal hard X-ray source (see Fig. 12) is located inside the system of flare loops (collapsing magnetic traps) in the upper part of this system and partly above it. To describe it, we use the thin-target approximation (see Section 2.3). We list the parameters available from observations. We believe that the coronal source is located in the immediate vicinity of the electron acceleration region and the high-temperature (superhot) reconnecting current layer (RCL in Fig. 2), and, according to estimates in [110], has an angular size of $\approx 15''$.

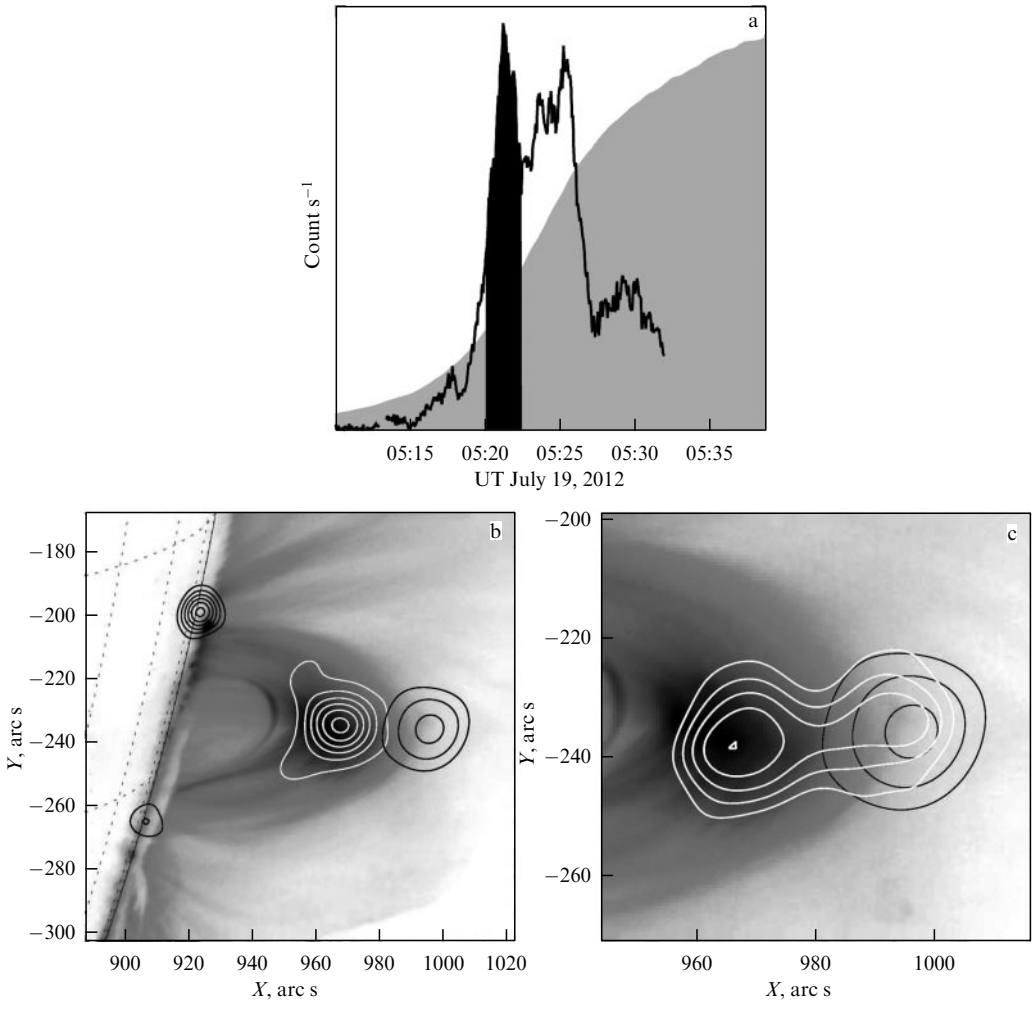


**Figure 12.** Flare on July 19, 2012. (a) Radiation intensity from the entire flare (black curve) according to RHESSI data in the range of 30–80 keV. Gray background — radiation intensity in the range of 3–25 keV according to GOES. (b, c) Background — images at a wavelength of 193 Å obtained with the SDO using the AIA ultraviolet telescope. System of flare loops with coronal and chromospheric sources is visible in (b), and coronal source, in (c). Black contours show the radiation levels according to the RHESSI data in the range of 30–80 keV. White contours are also drawn according to the RHESSI data: radiation levels in the ranges of (b) 6–8 keV and (c) 16–18 keV.

The lower edge of the energy spectrum of accelerated electrons is $\mathcal{E}_{\min} \approx 15$ keV. As noted, it is estimated with a significant error due to the superposition of the thermal and nonthermal injection spectra characteristic of any flare. This introduces inaccuracies into the determination of the intensity of hard X-rays, but has almost no effect on the estimate of the main observed parameter in the spectrum, its slope exponent. The upper edge of the spectrum is not known for certain. As previously, we conventionally set it equal to $\mathcal{E}_{\max} = 120$ keV.

We present estimates of other parameters of the July 19, 2012 flare taken from [110]. The temperature of the cold plasma in the target behind the turbulent front (see Fig. 2) is high, $T_2 \approx 21$ MK. The temperature of the source of energetic electrons, i.e., compact superhot plasma near the reconnection region, is unknown from observations and is assumed to be $T_1 \approx 100$ MK by order of magnitude. The plasma density in the coronal source is $n_2 \approx 3 \times 10^9$ cm$^{-3}$ (see Fig. 8.8 in [29]). The hard X-ray emission from a coronal source has the spectral slope exponent $\varphi_{\rm Cor} = 4.6 \pm 0.2$ with a flux 0.1 photon cm$^{-2}$ keV$^{-1}$ at an energy of 50 keV, and that from the chromospheric source, $\varphi_{\rm Ch} = 3.0 \pm 0.2$ with a flux of 1 photon cm$^{-2}$ keV$^{-1}$.

The observational (primarily spectral) characteristics of the hard X-ray emission of the July 19, 2012 flare presented in this section, as already noted, are the result of adding individual images over the time interval ($\sim 150$ s) of the first and largest radiation burst in the range of 30–80 keV. It was noted in Section 3.3 that several collapsing traps in the corona are created and destroyed during such a time interval (see Fig. 2), the effective lifetime of each of them being $\sim 5$ s [67]. Therefore, to interpret the observations, we have no choice but to tune the effective value of the mirror ratio $b_{\rm m}$ of the trap [92], unknown from observations, so as to fit the intensity of the hard X-ray emission in the corona to the observed one. In addition, it is necessary to estimate the compression parameters of such an 'averaged' trap in order to understand the individual roles of the Fermi acceleration and betatron heating in this flare.

**4.3.2 Hard X-ray spectrum.** The solid straight line in Fig. 13 shows the spectrum of hard X-ray emission from a chromospheric source in the flare on July 19, 2012, calculated in the thick-target model with a reverse current. It can be seen that the calculated spectrum agrees well with the results of observations of the chromospheric source (circles) in terms of both the radiation intensity and the spectrum slope. Therefore, model parameters such as the energy flux density $F$ carried by energetic electrons and the injection spectrum slope exponent $\gamma_{\rm v}$ are chosen correctly. As in Section 4.2, to compare the models, in Table 2 we also show the estimates derived in the approximation of the classical thick-target model without the reverse current.

The spectrum of the coronal source calculated in the thin-target approximation without taking the effect of collapsing magnetic traps into account is shown in Fig. 13 with a dotted line. It has the same slope as the observed coronal source

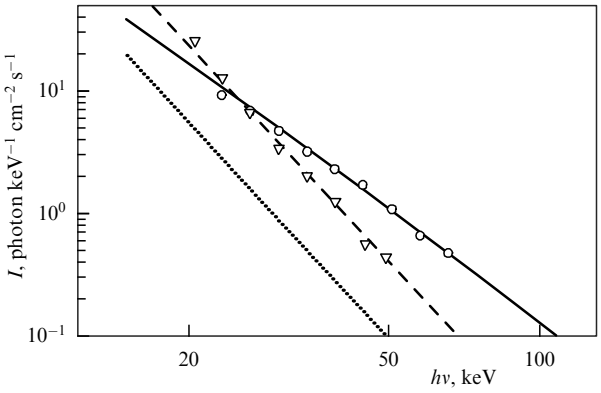


**Figure 13.** Observed and calculated spectra of hard X-ray emission from the solar flare of July 19, 2012. Results of the simulation of the chromospheric source are shown with a solid straight line, observations, by circles. Modeling of a coronal source without taking the acceleration of electrons in a collapsing magnetic trap into account (dotted line) and taking it into account (dashed line). Observational results are shown with triangles.

spectrum (triangles) but lies much lower. We therefore conclude that it is fundamentally impossible to simulate the observed spectra of coronal and chromospheric hard X-ray sources generated by a single population of accelerated electrons in the framework of the classical thin- and thick-target models.

Indeed, in the classical model, we always have $\varphi_{\rm Cor} - \varphi_{\rm Ch} = 2$ (formulas (50) and (51)), while flare observations yield $\varphi_{\rm Cor} - \varphi_{\rm Ch} \approx 1.6$ (see Table 2). In the reverse-current model, the observed ratio of the slope exponents follows naturally for the flare parameters specified in Section 4.3.1. Thus, the thick-target approximation with a reverse current not only accurately describes the X-ray spectrum of a chromospheric source but also allows finding the correct exponent of the emission spectrum slope in the corona.

An exception is the value of the radiation intensity of the coronal source (dashed straight line in Fig. 13), which in the model turns out to be lower than the observed one by about 4.5 times. Such a large discrepancy between the calculated and observed intensities, given the exact coincidence of the radiation spectrum slope exponents, is a weighty argument in favor of the presence and high efficiency of electron acceleration in collapsing magnetic traps formed by reconnected magnetic field lines (see Fig. 2). Such a picture of solar flares was predicted in theoretical studies [67, 92], but, to date, in the absence of high-resolution space experiments, no convincing observational confirmation has been available.

In accordance with the conclusions drawn in Section 3.3 on the possibility of estimating the characteristic parameters of an 'averaged' coronal trap, Eqn (46) was used in [72] to calculate the longitudinal ($l$) and transverse ($b$) compression coefficients in the July 19, 2012 flare. This then allowed a conclusion to be reached on the predominant acceleration mechanism and its effectiveness. We now discuss the results.

**Table 2.** Characteristics of electrons accelerated in the flare on July 19, 2012 in thick-target models with and without reverse current.

| Model | $\gamma_{\rm v}$ | $\gamma_{\mathcal{E}}$ | $\gamma_{\rm SS}$ | $n_{\rm b}$, cm$^{-3}$ | $F$, erg cm$^{-2}$ s$^{-1}$ | $\varphi_{\rm Cor}$ | $\varphi_{\rm Ch}$ |
|---|---|---|---|---|---|---|---|
| Without reverse current | 5.0 | 4.5 | 4.0 | $4.6 \times 10^7$ | $1.0 \times 10^{10}$ | 5.0(4.6) | 3.0(3.0) |
| With reverse current | 4.5 | 4.0 | 3.5 | $3.1 \times 10^8$ | $5.0 \times 10^{10}$ | 4.5(4.6) | 3.0(3.0) |

In the short time ($\sim$ 100 s) of the impulsive phase of the flare, the geometry of the reconnection region does not change [108]. Nevertheless, it occurs sufficiently rapidly to ensure the required power of energy release. New traps are quickly produced and then quickly collapse and disappear, but the general geometry of the system of collapsing traps represented by a 'total effective trap' seems to be unchanged or to vary slowly. We hence conclude that the flare under consideration was presumably dominated by transverse compression, i.e., the electrons were arguably accelerated via betatron heating.

In the general case, energetic electrons trapped in collapsing traps with dominant betatron heating are accelerated sooner [92], and the hard X-ray radiation generated by them in the corona has a much higher intensity (dashed line in Fig. 13). In addition, based on observational data, we can assume that, for many solar flares in such traps, the betatron acceleration due to their transverse compression prevails.

Apparently, in solar flares attended by powerful hard X-ray coronal sources, the decisive role is played by the additional acceleration of electrons in collapsing magnetic traps located above the chromosphere. Of course, the higher radiation intensity in the corona than in the classical flare model is related to increased emission not only due to the effective confinement and acceleration of electrons in collapsing coronal traps but also due to the effect of the reverse-current electric field.

**4.3.3 Spectrum of accelerated electrons and plasma heating power.** Three solar flares observed with high spatial and temporal resolution, including the flare on July 19, 2012 described above, are considered in [111]. They share the high-altitude position of the hard X-ray and optical radiation in the chromosphere. This cannot be explained within the classical thick-target model (also see [62, 104]). As in Section 4.2.3, in order to estimate the depth of electron penetration into the target and understand the features of electron propagation, we calculate the spectra of accelerated electrons and the plasma heating power.

The energy spectra of electrons accelerated in the July 19, 2012 flare during the impulsive phase in the largest burst of hard X-ray radiation (Fig. 12a) were calculated using formula (55) for two models and are shown in Figs 14. In the classical model of a thick target without reverse current (Fig. 14, curves *a*), the injection spectrum has the slope exponent $\gamma_{\mathcal{E}} \approx 4.5$, and the electron density calculated by formula (54) is $n_{\rm b} \approx 4.6 \times 10^7$ cm$^{-3}$. In the thick-target model with reverse current (Fig. 14, curves *b*), the injection spectrum is harder, $\gamma_{\mathcal{E}} \approx 4.0$, and the concentration is higher, $n_{\rm b} \approx 3.1 \times 10^8$ cm$^{-3}$.

We calculate the power of plasma heating by accelerated electrons in the target by formula (56). In the reverse-current model, the plasma heating pattern is very different from the results of calculations for the classical model without reverse current (Fig. 15) and is identical to that obtained in Section 4.2.3 for the December 6, 2006 flare. Higher layers of the chromosphere are heated more in the reverse-current model.

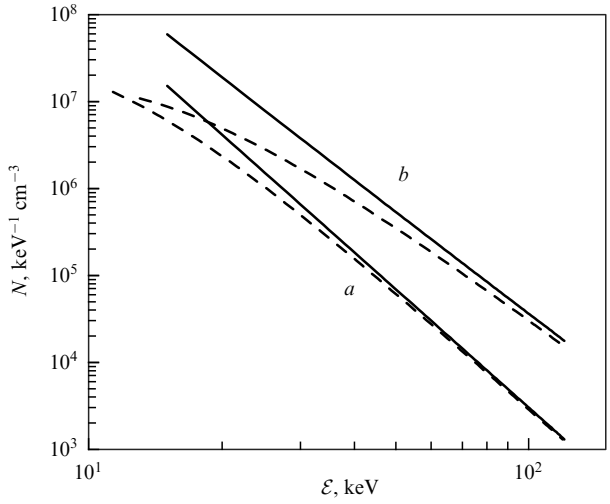


**Figure 14.** Differential energy spectra of accelerated electrons: (*a*) classical thick-target model without reverse current, (*b*) thick-target model with reverse current. Solid straight line is the injection spectrum, dashed line is the spectrum of electrons at plasma thickness $\xi = 3 \times 10^{19}$ cm$^{-2}$.

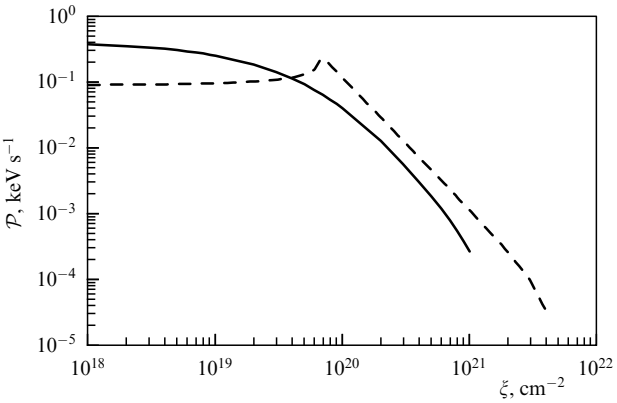


**Figure 15.** Power of plasma heating by accelerated electrons in the flare on July 19, 2012, calculated in the thick-target model: dashed line — without reverse current, solid line — with reverse current.

## 4.4 Polarization of hard X-ray radiation

**4.4.1 Calculations of polarization in solar flares**. In addition to the spectral slope exponent, the validity of the assumptions about the nature of the propagation of energetic electrons in the solar atmosphere during flares (i.e., the choice of a model) can be verified by calculating and comparing the radiation intensity and its boundaries with observational data. Apparently a less trivial and very sensitive task is to compare the theoretical predictions of hard X-ray polarization calculated in the framework of the corresponding models with data of satellite observations.

The general procedure for calculating the polarization of bremsstrahlung is presented, for example, in [100] (also see [45]). The polarization of hard X-ray radiation is defined as

$$P = \frac{I_\perp - I_\parallel}{I_\perp + I_\parallel}\,, \tag{57}$$

where the radiation fluxes $I_\perp$ and $I_\parallel$ are calculated in accordance with formulas (47) and (48); the radiation geometry is shown in Fig. 7 (see Section 4.1).

We calculate the polarization in the approximation of a two-dimensional velocity model of a thick target with a reverse current (see Section 3.2) [112]. The polarization is positive and takes very small values due to the weak anisotropy of distribution function (34). The highest polarization values of $\sim 3\%$ are achieved at the lowest photon energy values; as the energy increases, the polarization decreases monotonically. As the angle $\psi$ between the line of sight and the direction of propagation of the fast electron flow

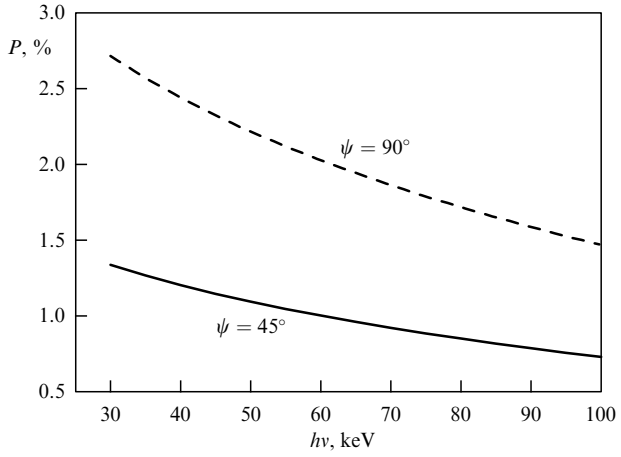


**Figure 16.** Polarization of hard X-rays near the boundary of a thick target as a function of the photon energy $h\nu$ at various values of angle $\psi$. The calculations were done with $\gamma_{\mathbf{v}} = 4$ and $F = 10^{11}$ erg cm$^{-2}$ s$^{-1}$.

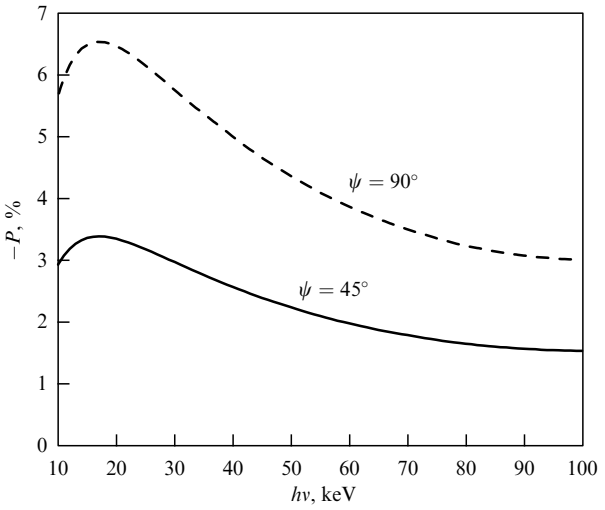


**Figure 17.** Polarization of hard X-ray bremsstrahlung generated by superhot runaway electrons as a function of the photon energy $h\nu$ at various values of angle $\psi$ (see [82] for details).

(the $x$-axis in Fig. 3) decreases, the polarization also decreases (Fig. 16).

Strictly speaking, the result obtained is valid for depths in the target where the reverse-current electric field is $\varepsilon \gg 1$. At greater depths, the distribution function should become the one it was in the two-dimensional collision model. However, the number of energetic electrons at these depths is much less than the initial one, and therefore the main contribution to the polarization of radiation comes from electrons near their source. The degree of polarization is then virtually independent of the thickness. This is considered in more detail in [66].

It is also important that, according to modern observations of hard X-ray radiation, the energy $h\nu \approx 15$ keV lies in the spectrum region where the nonthermal and thermal bremsstrahlung components are superimposed (see, e.g., [33]). This means that the polarization can be determined not only by accelerated electrons with a power-law spectrum but also by superhot (thermal) electrons (see Section 2.5), whose spectrum differs little from the Maxwellian one.

The polarization of hard X-ray radiation generated by thermal runaway electrons is calculated with distribution function (19); the results are shown in Fig. 17. According to these calculations, the maximum bremsstrahlung polarization of the superhot runaway electrons can reach 6% at the photon energy $h\nu \approx 15$ keV. However, the polarization could have become so large if the angle $\psi = 90°$ between the line of sight and the direction of propagation of superhot electrons. Given the heliocentric distribution of solar flares, we must choose the more probable value $\psi \approx 45°$ and therefore take the most probable bremsstrahlung polarization value $P \lesssim 3-4\%$ for runaway superhot electrons. Such low values of X-ray polarization ($\lesssim 3\%$) are quite natural and are related to two circumstances.

First, the distribution function of energetic electrons (superhot and accelerated) cannot be strongly anisotropic in solar flares. If all the electrons that generate the hard X-ray emission of the flare were directed in one direction, then the electric current carried by them (see (3))

$$J(r) = Sj(r) = Se \int f_{\mathbf{v}}(r, v, \theta)\, v \cos\theta \, \mathrm{d}\mathbf{v}\,,$$

where $S$ is the cross-sectional area of the flow of energetic electrons, would take a huge value $10^{17}$–$10^{18}$ A [63]. Real currents in a flare, including at its energy source, are $10^{11}$–$10^{12}$ A [113]. Consequently, the degree of anisotropy of energetic electrons does not exceed $10^{-6}$–$10^{-5}$. Energetic electrons must then already be almost isotropic in the flare energy source. Even in the presence of small initial anisotropy, the distribution function is rapidly made isotropic with increasing depth under the action of the reverse-current electric field (see [66, Section 5]).

Second, for superhot and accelerated electrons, whose energy is much higher than the energy of thermal plasma electrons, we can ignore the energy in the kinetic equation compared to regular energy losses in Coulomb collisions, but cannot ignore angular diffusion (see [28, § 4.2]). Angular diffusion is relevant in the same order of magnitude as regular energy losses:

$$\cos\theta \, \frac{\partial f_{\mathbf{v}}}{\partial \xi} = \frac{1}{z} \, \frac{\partial f_{\mathbf{v}}}{\partial z} + \frac{1}{2z^2} \, \Delta_\theta f_{\mathbf{v}}\,.$$

The greater the energy loss, the faster the distribution function of energetic electrons is driven isotropic by angular diffusion.

We compare Figs 16 and 17. It is easy to see that the polarizations of X-rays generated by thermal and nonthermal electrons differ in sign and absolute value. To explain this, we must compare distribution functions (34) and (19) using the expressions for the cross sections of bremsstrahlung polarized parallel and perpendicular to the $Q_\parallel$ plane [100] (see Fig. 7).

As we have noted, the anisotropy of function (34) at the target boundary is small, being caused by backward electrons (the distribution of forward particles was assumed to be isotropic; see Section 2). Under the action of the reverse-current electric field, this distribution function rapidly becomes isotropic as the depth of penetration into the target increases, implying low values of the polarization of the X-ray bremsstrahlung generated by such electrons. In the electric fields $\varepsilon \gtrsim 1$, distribution function (34) contains a large number of particles with pitch-angle cosine values $|\mu| \ll 1$, whence $I_\perp - I_\parallel > 0$ (see formula (3.11) in [100]), and the expected polarization of the generated radiation is positive.

Near the target boundary, function (19) describes isotropically distributed forward electrons (there are no particles moving in the opposite direction), and its evolution is determined solely by Coulomb collisions. Therefore, as the depth increases, this function decreases more slowly, becoming more directed ($\mu \sim 1$). At a large thickness (the third case in expression (19)), the function becomes isotropic. These features provide a negative value of the radiation polarization.

The models proposed here for the propagation of accelerated and superhot electrons do not account for a number of factors that are characteristic of the real conditions of a solar flare and reduce the degree of anisotropy of the energetic electron flux (see an overview of the problem in [62]). Their bremsstrahlung polarization also diminishes. One of the factors is the Compton scattering of hard X-rays by the photosphere [114, 115].

The effect of Compton scattering in the photosphere on the directivity and polarization of X-rays in the range of 15–150 keV was calculated by the Monte Carlo method in [114]. It was shown that, for an isotropic source of X-ray photons in the corona, the total polarization of radiation in Earth's orbit does not exceed 4%. This conclusion is quite close to our results, because the energetic electron distribution function that we found differs little from the isotropic one, and therefore the primary X-ray emission from the flare is almost isotropic, which was assumed in [114].

We emphasize, however, that we were solving a different problem. Our approach to the question of the possible polarization of hard X-ray emission from flares is fundamentally different from that in [114, 115]. We do not fix the primary X-ray flux, but calculate it based on the solution of the kinetic equation for the distribution function of energetic electrons. We have shown that the polarization of their bremsstrahlung does not exceed 4%, which formally coincides with the result in [114]. However, it remains to be seen how much the Compton scattering of primary X-ray radiation on the photosphere reduces the polarization of the total radiation flux observed in Earth's orbit. The observed polarization may well be closer to that predicted in [115].

**4.4.2 Polarization observations in solar flares.** The first attempts to measure the polarization of hard X-rays in solar flares have apparently not been entirely successful, because the measured polarization degree turned out to be comparable to the measurement errors (see [116, 117]). For example, at the energy $h\nu = 15$ keV, measurements aboard the Interkosmos series satellites (1969–1974) showed a high degree of polarization, $P = 40\%$, with very large measurement errors (see Fig. 2 in [116]). In addition, a high degree of polarization was observed for such a long time that it could not be explained by electrons accelerated in the flare, and no other explanation has been offered.

Attempts to observe polarization aboard the OSO-7 satellite (1972) in the energy range $h\nu = 15$–30 keV were unsuccessful due to malfunctions of the polarimeter. Direct measurement of the polarization turned out to be impossible, but it was nevertheless possible to obtain a lower estimate of the absolute value of the polarization degree $|P| = 10$–20% [118]. As in the Interkosmos measurements, the long-term existence of significant polarization was found, much longer than the thermalization time of accelerated electrons in the flare plasma [119].

Polarization measurements in the range $h\nu = 20$–100 keV were carried out aboard the domestic device KORONAS-F (2001–2005) using the SPR-N polarimeter. For 25 flares, estimates of the upper bound of the polarization degree $|P| = 8$–40% were obtained [120]. For the flare on October 29, 2003, extremely large polarization values were obtained, more than 70%, but errors in these measurements are quite high (see Fig. 4 in [120]).

Observing radiation polarization in the same range was also made possible by the equipment aboard the RHESSI satellite (2002–2019) [121]. However, the sensitivity of the polarimeter turned out to be insufficient, and no results were obtained with undoubted reliability [122]. Apparently, more successful were measurements of the polarization of gamma radiation, $h\nu = 0.2$–1 MeV, in two large flares: $P = 21 \pm 9\%$ in a class X4.8 flare on July 23, 2002, and $P = -11 \pm 5\%$ in a class X17 flare on October 28, 2003 [123].

Half a century has passed since the first polarization measurements, but little change has occurred. As the accuracy of polarimetric observations has increased, the recorded degree of polarization has decreased, but the reliability of the data obtained has remained, strictly speaking, unconfirmed.

**4.4.3 Future experiments to measure polarization.** What should be taken into account when planning future experiments to measure the polarization of hard X-ray emission from solar flares and interpreting future results? In general, we see that estimates of the expected maximum polarization obtained for superhot and accelerated electrons in the energy range of 15–100 keV are within 3 to 4%. Therefore, polarization measurements with an accuracy of the order of 1% are needed.

Promising instruments for measuring polarization in solar flares are discussed in review [124]. The first of them, the Gamma-Ray Imager/Polarimeter for Solar flares (GRIPS [125]), has good spectral and angular resolution, but the minimum measurable polarization is $\sim 3\%$, and the energy is $\sim 150$ keV. This telescope is not suitable for studying solar flares and, in particular, for measuring the polarization of X-rays in the range of 10–100 keV. For this energy range, the Sapphire polarimeter (Solar Polarimeter for Hard X-rays [126]), which should provide a minimum measured polarization value of $\sim 1.5\%$, can be considered more suitable. The Japanese X-ray polarimeter [127], which will operate in the 60–300-keV range, is planned to be launched in 2025. Other existing polarimeters (for example, Imaging X-ray Polarimetry Explorer, IXPE [128] and POLAR [129]) have sensitivities two orders of magnitude higher than that of RHESSI, but they are not aimed at studying solar flares but cosmic gamma-ray bursts, which are the brightest electromagnetic events occurring in the Universe. Polarization measurements will complement the results of spectral observations that will be obtained in the framework of the joint Russian–German Spektr–Roentgen–Gamma (Spektr-RG) space observatory.

Future measurements of the polarization of hard X-rays and gamma rays from solar flares will be of great importance. Simultaneous spectral and polarization observations, together with the acquisition of images of solar flares in the energy range $h\nu \approx 10$–100 keV, will allow an experiment-based answer to the key questions in the physics of a wide class of flares of an electromagnetic nature, not only on the Sun but also on other stars with strong magnetic fields: (1) magnetic reconnection as the primary mechanism for accelerating electrons and ions, (2) reconnection as a mechanism for heating plasma to enormous temperatures,

(3) additional mechanisms for particle acceleration and plasma heating in flares.

In the framework of the Interhelioprobe international project [130], it is planned to use the PING-P polarimeter [131] in the range of 18–150 keV, which, with an X-ray flux of 1500 photons $cm^{-2}$ in that range (typical flux for class-X1 flares), will provide the minimum measurable polarization $P_{min} = 2.9\%$ at the $3\sigma$ level with a 10-s time resolution. At higher radiation fluxes (for flares of a class higher than X1), it will be possible to achieve even higher sensitivity and accuracy of polarization measurements. It can be hoped that this will allow answering the questions posed above in the physics of solar flares, which are closely related to the fundamental process of magnetic reconnection in a plasma with a strong magnetic field.

In the longer term, it is desirable to focus on projects of space observatories designed for continuous monitoring of solar activity, including measurements of the spectrum and polarization of X-ray and gamma-ray flares, as well as accompanying measurements of the composition and characteristics of charged particles and the solar wind plasma. To solve this complex experimental problem, evidently, a stable location of the space observatory at the Sun–Earth L1 Lagrange point is required.

## 5. Conclusion

Observations of solar flares in the course of ground-based and space experiments of the last decade have generally confirmed the classical ideas about the nature of their occurrence, evolution, and impact on interplanetary space. At the same time, the classical models of the primary acceleration of charged particles and the description of the plasma flow in the vicinity of the magnetic reconnection region, as well as secondary processes associated with the heating of the surrounding plasma, additional particle acceleration, and radiation, still require refinement and accurate quantitative interpretation.

The kinetic models of a flare discussed in this paper, which include the secondary acceleration and propagation of charged particles in the solar atmosphere, correspond to the current state of theory and observations and are quite suitable for calculating the characteristics of X-ray bremsstrahlung. We nevertheless note possible directions for their further development, with regard to future experiments.

First of all, it is necessary to test the models of additional acceleration of electrons in coronal magnetic traps in a large number of flare events for which the angular resolution of X-ray observations is within $1'$ and the time resolution is $\sim 1$ s. The question of the initial angular distribution of injected energetic electrons, which directly affects the measured radiation polarization, remains open. Finally, modern developments in ground-based optical observations show great promise for obtaining tomographic cross sections of active regions and flares, which would allow detecting velocity fields at different levels in the solar atmosphere.

The reverse-current thick-target model can be a reliable basis for studying the 'white flare' phenomenon. For this, it is necessary to carefully study the hydrodynamic response of the chromosphere to pulsed heating by such large fluxes of energetic electrons. Recall that they are 1 to 2 orders of magnitude higher than the values predicted by classical thick-target models.

The presence of strong magnetic fields, high temperatures, plasma flow densities and velocities, and powerful heat fluxes, together with the possibility of high-precision observations in the entire electromagnetic spectrum, make the Sun a natural laboratory for studying fundamental physical processes. This allows using the results of solar flare and solar activity studies in general to solve a wider range of astrophysical problems where the key role is played by the effect of magnetic reconnection in a strong magnetic field and its most important consequences: the acceleration and propagation of charged particles, their electromagnetic radiation in various spectral ranges, and high-speed directed flows of high-temperature plasma.

## References


1. Smith H J, Smith E V P *Solar Flares* (New York: Macmillan, 1963)
2. Švestka Z *Solar Flares* (Dordrecht: D. Reidel, 1976)
3. Somov B V "Vspyshka na Solntse" ("Solar flare"), in *Fizicheskaya Entsiklopediya* (Physical Encyclopedia) Vol. 1 (Ed.-in-Chief A M Prokhorov) (Moscow: Sovetskaya Entsiklopediya, 1988) p. 350
4. Aschwanden M *Physics of the Solar Corona: An Introduction with Problems and Solutions* (Berlin: Springer-Verlag, 2005)
5. Fletcher L et al. *Space Sci. Rev.* **159** 19 (2011)
6. Somov B V *Nauka Zhizn* (8) 11 (2007)
7. Howard T *Coronal Mass Ejections: An Introduction* (Berlin: Springer, 2011)
8. Hanslmeier A *The Sun and Space Weather* (Dordrecht: Springer, 2007)
9. Lilensten J *Space Weather* (Dordrecht: Springer, 2007)
10. Pilipenko V A et al. *Izv. Phys. Solid Earth* **54** 721 (2018); *Fiz. Zemli* (5) 61 (2018)
11. Zhang J et al. *Earth-affecting Solar Transients* (Berlin: Springer, 2019)
12. Somov B V, Syrovatskii S I *Sov. Phys. Usp.* **19** 813 (1976); *Usp. Fiz. Nauk* **120** 217 (1976)
13. Somov B V *Physical Processes in Solar Flares* (Dordrecht: Springer, 1992)
14. Feng L et al. *Astrophys. J.* **765** 37 (2013)
15. Aschwanden M J et al. *Astrophys. J.* **832** 27 (2016)
16. Chen B et al. *Bull. Am. Astron. Soc.* **51** 507 (2019)
17. Giovanelli R G *Mon. Not. R. Astron. Soc.* **108** 163 (1948)
18. Parker E N *J. Geophys. Res.* **62** 509 (1957)
19. Dungey J W *Cosmic Electrodynamics* (Cambridge: Cambridge Univ. Press, 1958)
20. Sweet P A *Nuovo Cimento* **8** 188 (1958)
21. Syrovatskii S I *Sov. Astron.* **6** 768 (1963); *Astron. Zh.* **39** 987 (1962)
22. Syrovatskii S I *Sov. Astron.* **10** 270 (1966); *Astron. Zh.* **43** 340 (1966)
23. Sweet P A *Annu. Rev. Astron. Astrophys.* **7** 149 (1969)
24. Masuda S et al. *Nature* **371** 495 (1994)
25. Narukage N, Shimojo M, Sakao T *Astrophys. J.* **787** 125 (2014)
26. Cairns I H et al. *Sci. Rep.* **8** 1676 (2018)
27. Priest E, Forbes T *Magnetic Reconnection: MHD Theory and Applications* (Cambridge: Cambridge Univ. Press, 2000)
28. Somov B V *Plasma Astrophysics* Pt. 1 *Fundamentals and Practice* 2nd ed. (New York: Springer, 2012)
29. Somov B V *Plasma Astrophysics* Pt. 2 *Reconnection and Flares* 2nd ed. (New York: Springer, 2013)
30. Krucker S et al. *Astron. Astrophys. Rev.* **16** 155 (2008)
31. Zharkova V V et al. *Space Sci. Rev.* **159** 357 (2011)
32. Emslie A G et al. *High-Energy Aspects of Solar Flares* (New York: Springer-Verlag, 2012)
33. Benz A O *Living Rev. Sol. Phys.* **14** 2 (2017)
34. Fleishman G D et al. *Science* **367** 278 (2020)
35. Hudson H S, Ryan J *Annu. Rev. Astron. Astrophys.* **33** 239 (1995)
36. Somov B V *Cosmic Plasma Physics* (Dordrecht: Kluwer Acad. Publ., 2000)
37. Aschwanden M J *Particle Acceleration and Kinematics in Solar Flares* (Dordrecht: Kluwer Acad. Publ., 2002)
38. Miroshnichenko L *Solar Cosmic Rays: Fundamentals and Applications* 2nd ed. (Astrophysics and Space Science Library, Vol. 405) (Cham: Springer, 2015)
39. Casolino M et al. *Nucl. Phys.* **190** 293 (2009)
40. Bruno A et al. *Astrophys. J.* **862** 97 (2018)

41. Somov B V *Astron. Rep.* **55** 962 (2011); *Astron. Zh.* **88** 1045 (2011)
42. Somov B V *Astron. Lett.* **37** 679 (2011); *Pis'ma Astron. Zh.* **37** 679 (2011)
43. Bezrodnykh S I, Somov B V *Adv. Space Res.* **56** 2779 (2015)
44. Becker W *Neutron Stars and Pulsars* (Berlin: Springer-Verlag, 2009)
45. Fleishman G D, Toptygin I N *Cosmic Electrodynamics*: *Electrodynamics and Magnetic Hydrodynamics of Cosmic Plasmas* (Astrophysics and Space Science Library, Vol. 388) (New York: Springer, 2013)
46. Balogh A et al. *Particle Acceleration in Cosmic Plasmas* (Space Sciences Ser. of ISSI, Vol. 45) (New York: Springer, 2013)
47. Ginzburg V L, Syrovatskii S I *The Origin of Cosmic Rays* (New York: Macmillan, 1964); Translated from Russian: *Proiskhozhdenie Kosmicheskikh Luchei* (Moscow: Izd. AN SSSR, 1963)
48. Dorman L *Cosmic Rays in Magnetospheres of the Earth and other Planets* (Dordrecht: Springer, 2009)
49. Shalchi A *Nonlinear Cosmic Ray Diffusion Theories* (Berlin: Springer-Verlag, 2009)
50. Syrovatskii S I, Shmeleva O P, in *Solar Terrestrial Relations, Proc. of the Conf.* (Ed. D Venkatesan) (Calgary: Univ. of Calgary Press, 1973)
51. Shih A Y, Lin R P, Smith D M *Astrophys. J. Lett.* **698** L152 (2009)
52. Lin R P et al. *Solar Phys.* **210** 3 (2002)
53. Lemen J R et al. *Solar Phys.* **275** 17 (2012)
54. Müller D et al. *Solar Phys.* **285** 25 (2013)
55. Chen B et al. *Astrophys. J.* **908** L55 (2021)
56. Sui L, Holman G D, Dennis B R *Astrophys. J.* **612** 546 (2004)
57. Dennis B R et al. *Astrophys. J.* **867** 82 (2018)
58. Aschwanden M *Solar Phys.* **383** 210 (2002)
59. Young P R et al. *Astron. Astrophys.* **495** 587 (2009)
60. Brown J C *Solar Phys.* **18** 489 (1971)
61. Syrovatskii S I, Shmeleva O P *Sov. Astron.* **16** 273 (1972); *Astron. Zh.* **49** 334 (1972)
62. Gritsyk P A, Somov B V *Astron. Lett.* **40** 499 (2014); *Pis'ma Astron. Zh.* **40** 554 (2014)
63. Hoyng P, van Beek H F, Brown J C *Solar Phys.* **48** 197 (1976)
64. Zhu R et al. *Sci. China Technol. Sci.* **64** 169 (2021)
65. Diakonov S V, Somov B V *Solar Phys.* **116** 119 (1988)
66. Litvinenko Yu E, Somov B V *Solar Phys.* **131** 319 (1991)
67. Somov B V, Kosugi T *Astrophys. J.* **485** 859 (1997)
68. Sakai J I, de Jager C *Cosmic Plasma Physics* (Dordrecht: Kluwer Acad. Publ., 1996)
69. Lin R P, Hudson H S *Solar Phys.* **17** 412 (1971)
70. Leach J, Petrosian V *Astrophys. J.* **251** 781 (1981)
71. Gritsyk P A, Somov B V *Astron. Lett.* **42** 531 (2016); *Pis'ma Astron. Zh.* **42** 586 (2016)
72. Gritsyk P A, Somov B V *Astron. Lett.* **43** 614 (2017); *Pis'ma Astron. Zh.* **43** 676 (2017)
73. Allred J C et al. *Astrophys. J.* **902** 16 (2020)
74. Somov B V *Izv. Akad. Nauk SSSR Ser. Fiz.* **45** 576 (1981)
75. Brown J C, Spicer D S, Melrose D B *Astrophys. J.* **228** 592 (1979)
76. van den Oord G H J *Solar Phys.* **234** 496 (1990)
77. Alaoui M et al. *Astrophys. J.* **917** 74 (2021); arXiv:2103.13999
78. Battaglia M, Kontar E P *Astrophys. J.* **760** 142 (2012)
79. Brown J C *Solar Phys.* **26** 441 (1972)
80. Ramaty R *Astrophys. J.* **158** 753 (1969)
81. Holt S S, Ramaty R *Solar Phys.* **8** 119 (1969)
82. Gritsyk P A, Somov B V *J. Exp. Theor. Phys.* **129** 935 (2019); *Zh. Eksp. Teor. Fiz.* **156** 1016 (2019)
83. Kontar E P et al. *Astrophys. J.* **809** 35 (2015)
84. Knight J W, Sturrock P A *Solar Phys.* **218** 306 (1977)
85. Sermulyn'sh V A, Somov B V, in *Kompleksnoe Izuchenie Solntsa*: *Trudy XII Leningradskogo Seminara po Kosmofizike* (Complex Study of the Sun: Proc. of the XII Leningrad Seminar on Cosmophysics) (Eds V A Dergachev, G E Kocharov) (Leningrad: RTP LIYaF, 1982) p. 90
86. Vladimirov V S *Equations of Mathematical Physics* (Moscow: Mir, 1984); Translated from Russian: *Uravneniya Matematicheskoi Fiziki* (Moscow: Nauka, 1981)
87. Gritsyk P A, Somov B V *Moscow Univ. Phys. Bull.* **66** 466 (2011); *Vestn. Mosk. Univ. Ser. 3. Fiz. Astron.* (5) 56 (2011)
88. Dennis B R, Emslie A G, Hudson H S *Space Sci. Rev.* **159** 3 (2011)
89. Hudson H S *Solar Phys.* **291** 1273 (2016)
90. Somov B V, Bogachev S A *Astron. Lett.* **29** 621 (2003); *Pis'ma Astron. Zh.* **29** 701 (2003)
91. Bogachev S A, Somov B V *Astron. Lett.* **31** 537 (2005); *Pis'ma Astron. Zh.* **31** 601 (2005)
92. Bogachev S A, Somov B V *Astron. Lett.* **33** 54 (2007); *Pis'ma Astron. Zh.* **33** 62 (2007)
93. Emslie A G *Astrophys. J.* **235** 1055 (1980)
94. Kuridze D et al. *Astrophys. J.* **874** 126 (2019)
95. Spitzer L *Physics of Fully Ionized Gases* (New York: Interscience Publ., 1965)
96. Effenberger F et al. *Astrophys. J.* **835** 124 (2017)
97. Kosugi T et al. *Solar Phys.* **243** 3 (2007)
98. Goodman S J et al., in *Comprehensive Remote Sensing* (Ed. S Liang) (Amsterdam: Elsevier, 2018) p. 119
99. Handy B N et al. *Solar Phys.* **187** 229 (1999)
100. Elwert G, Haug E *Solar Phys.* **15** 234 (1970)
101. Nocera L et al. *Solar Phys.* **97** 81 (1985)
102. Huang N-Y, Xu Y, Wang H *Res. Astron. Astrophys.* **16** 177 (2016)
103. Namekata K et al. *Astrophys. J.* **851** 91 (2017)
104. Krucker S et al. *Astrophys. J.* **739** 96 (2011)
105. Tsuneta S et al. *Astrophys. J.* **478** 787 (1997)
106. Caspi A, Krucker S, Lin R P *Astrophys. J.* **781** 43 (2014)
107. Oreshina A V, Somov B V *Astron. Lett.* **37** 726 (2011) *Pis'ma Astron. Zh.* **37** 789 (2011)
108. Liu W, Chen Q, Petrosian V *Astrophys. J.* **767** 168 (2013)
109. Liu R *Mon. Not. R. Astron. Soc.* **434** 1309 (2013)
110. Krucker S, Battaglia M *Astrophys. J.* **780** 107 (2014)
111. Krucker S et al. *Astrophys. J.* **802** 19 (2015)
112. Gritsyk P A, Somov B V *Moscow Univ. Phys. Bull.* **67** 102 (2012); *Vestn. Mosk. Univ. Ser. 3. Fiz. Astron.* (1) 106 (2012)
113. Gopasyuk S I *Adv. Space Res.* **10** 151 (1990)
114. Henoux J C *Solar Phys.* **42** 219 (1975)
115. Mandelshtam S L, Beigman I L, Tindo I P *Nature* **254** 462 (1975)
116. Tindo I P, Somov B V, in *New Instrumentation for Space Astronomy, Proc. of a Symp. of the 20th Meeting of the COSPAR* (Eds K Van der Hucht, G S Vaiana) (Oxford: Pergamon Press, 1978) p. 131
117. Somov B V, Tindo I P *Cosmic Res.* **16** 555 (1979); *Kosmich. Issled.* **16** 686 (1978)
118. Thomas R J, in *Solar Gamma-, X-, and EUV Radiation* (IAU/COSPAR Symp. No. 68, Ed S R Kane) (Dordrecht: Reidel Publ., 1975) p. 25
119. Maran S P, Thomas R J, in *The New Astronomy and Space Science Reader* (Eds J C Brandt, S P Maran) (San Francisco: W H Freeman and Co., 1977) p. 293
120. Zhitnik I A et al., in *Solnechno-Zemnaya Fizika*: *Rezul'taty Eksperimentov na Sputnike KORONAS-F* (Solar-Terrestrial Physics: The Results of Experiments on the KORONAS-F Satellite) (Ed. V D Kuznetsov) (Moscow: Fizmatlit, 2009) p. 128
121. McConnell M L et al. *Solar Phys.* **210** 125 (2002)
122. McConnell M L et al. *Adv. Space Res.* **34** 462 (2004)
123. Boggs S E, Coburn W, Kalemci E *Astrophys. J.* **638** 1129 (2006)
124. Jeffrey N L S, Saint-Hilaire P, Kontar E P *Astron. Astrophys.* **642** A79 (2020)
125. Duncan N et al. *Proc. SPIE* **9905** 99052Q (2016)
126. Saint-Hilaire P et al., in *AGU Fall Meeting Abstracts* (2019) SH31C-3310
127. Narukage N *Am. Astron. Soc. Meeting Abstracts* **234** 12603 (2019)
128. Waisskopf M C et al. *Proc. SPIE* **9905** 990517 (2016)
129. Produit N et al. *Nucl. Instrum. Meth. Phys. Res. A* **877** 259 (2018)
130. Kuznetsov V D et al. *Geomagn. Aeron.* **56** 781 (2016)
131. Kotov Yu D et al. *Adv. Space Res.* **58** 635 (2016)